Table of Contents

I. FISCHER-TROPSCH SYNTHESIS ON IRON CATALYSTS

1. Background

1.1. Structure and Function of Active Phases in Fischer-Tropsch Synthesis

Fe-based oxides have been used as commercial catalysts for Fischer-Tropsch synthesis (FTS) to produce a large variety of paraffin and olefin products, ranging from methane to high molecular weight waxes [1]. During activation by synthesis gas and subsequent FTS reaction, several phases including metallic iron, iron carbides and iron oxides are known to co-exist at steady-state conditions [2-5]. The distribution and amounts of these phases depend on exposure to various activation and reaction conditions, leading to different catalytic performances in FTS. Some researchers [6] have proposed that surface iron atoms are responsible for FTS activity, while some others considered surface carbides or a mixture of carbides [7,8] and metallic iron [9] to be the active phase. There are also some reports that suggest that magnetite Fe_3O_4 is the active phase in FTS [10-12]. Although these studies have each provided some evidence to support their specific proposals about the active phase, the available information remains phenomenological, and a method to identify the active phase during reaction and to count the number of active sites has not yet been established.

Based on the previous research on Co [13,14] and Fe catalysts [15,16] for FTS as well as our last quarterly work on TPSR of Fe oxides in H_2, our characterization during this research period involved temperature-programmed reactions of Fe-based catalysts with flowing streams of CO or H_2-CO mixtures. We monitored the gas phase concentrations throughout the reduction and carburization processes by means of an on-line mass spectrometer, and followed the evolution of bulk phases and crystal size by X-ray diffraction and of surface area by nitrogen physisorption measurements. In this way, we can determine the temperature required for the formation of Fe carbides as well as the stoichiometry and structure of such carbides. Our goal is to develop a new synthesis method to improve the compositional and structural purity of Fe carbides formed, and consequently to refine the structure-function relationships that we have previously proposed to interpret the catalytic behavior of Fe-based catalysts.

1.2. Effects of Zn, K and Cu

Many components have been added to Fe catalysts in order to improve their mechanical and catalytic properties. Our previous studies have shown that zinc, alkali and copper [16,17] promote the catalytic properties of Fe oxides. Zinc oxide, as a non-reducible oxide in FTS conditions, appears to stabilize the surface area of Fe oxide. Alkali, as a modifier of the adsorption enthalpies of H_2 and CO, increases the selectivity to desired C_{5+} products. Copper promotes the carburization processes and decreases the temperature required for the activation of iron oxide. Here, our efforts have focused on Fe-Zn-K-Cu catalysts. We have prepared a series of Zn and Fe co-precipitated oxides with varied Zn/Fe ratios and then introduced varying amounts of K and Cu. We are examining the surface area, bulk structure, required reduction and carburization temperatures as well as the catalytic behavior of these catalysts, in order to identify optimum Zn/Fe ratios and Cu and K contents that give maximum site density and catalytic activity.

2. Synthesis Procedures for Fe-Zn-K-Cu Oxides

All catalysts were prepared by co-precipitation of zinc and iron nitrates at a constant pH of 7.0 in order to form porous mixed oxides. Then, these oxide precursors were impregnated with an aqueous solution of potassium and copper salts using incipient wetness methods. The Zn/Fe oxide precursors were prepared first. Fe nitrate (1.4 M) and Zn nitrate (3.0 M) solutions were mixed at a given atomic Zn/Fe ratio. A solution of ammonium carbonate (1 M) was prepared separately. Deionized water (ca. 50 ml) was added into a large flask, which was heated on a hot plate with a magnetic stirrer and held at 80 ^{o}C throughout the preparation process. The mixed Zn/Fe solution was added at 2 cm^3/min flow into the flask through a feeding pump. At the same time, the ammonium carbonate solution was fed separately, and its flow was controlled to maintain the slurry pH at 7±0.1, as monitored by a pH meter. The resulting precipitates were washed several times with about 1 *li* water per gram of catalyst, dried at 120 ^{o}C overnight, and then calcined at 350 ^{o}C for 1 h. The calcined material was promoted with 2 at.% K using K_2CO_3 solution (0.16 M) by incipient wetness and then dried. The same process was repeated in order to promote samples with 1 at.% Cu using $Cu(NO_3)_2$ solutions (0.16 M). Finally, the dried material was treated in dry air at 400 ^{o}C for 4 h. This final calcination temperature was chosen from temperature-programmed oxidation data, which showed that this temperature is sufficient to decompose all metal nitrates and carbonates except K_2CO_3. The catalysts contain CuO, ZnO, Fe_2O_3 and K_2CO_3. These catalysts were pressed at 443 MPa into pellets, lightly crushed, and then sieved to retain the 80-140 mesh fraction for FTS reaction.

3. Catalyst Characterization

3.1. Protocols for the Characterization of Fe-based FTS Catalysts

This research program addresses the synthesis and the structural and catalytic characterization of active sites in Fe-based catalysts for FTS. We have designed a matrix of samples that contains a systematic range of multi-components catalysts in order to determine the number and type of surface sites present on fresh catalysts and on samples during and after FTS reaction (Table 1.1). Our objective is to develop rigorous relationships between the synthesis methods, the resulting catalyst structures, and their function in FTS reactions.

3.2. In-Situ X-ray Absorption (XAS) Studies on Fe Catalysts

In-situ X-ray absorption near edge (XANES) and extended X-ray absorption fine structure (EXAFS) analyses provide us with the information about the oxidation states and the local structure of catalysts during FTS. In this reporting period, we continued our X-ray absorption studies at the Stanford Synchrotron Radiation Laboratory (SSRL) with emphasis on Fe K-edge measurements on our standard samples and on a series of fresh and used Fe-Si catalysts provided by Dr. Burtron A. Davis at the Center for Applied Energy Research (CAER) of University of Kentucky (abbreviated as CAER's sample hereafter).

Table 1.1. Matrix of Fe-Zn-K-Cu samples and characterization methods for FTS reaction

<table>
<tr><th colspan="3">Nominal Composition of the Catalysts</th><th rowspan="2">Characterization Before and After FTS</th><th rowspan="2">FTS reaction</th></tr>
<tr><th>Zn/Fe mole ratio</th><th>K/(Fe+Zn) (at.%)</th><th>Cu/(Fe+Zn) (at.%)</th></tr>
<tr><td rowspan="6">0</td><td rowspan="2">0</td><td>0</td><td rowspan="19">XRD

Surface area

In-situ XAS

H_2-TPR

CO-TPR</td><td rowspan="19">Effect of reaction condition

220 ^oC
21.4 atm

235 ^oC
21.4 atm

270 ^oC
5 atm

Effect of CO_2 addition

Isotopic studies</td></tr>
<tr><td>1</td></tr>
<tr><td rowspan="3">2</td><td>0</td></tr>
<tr><td>1</td></tr>
<tr><td>2</td></tr>
<tr><td>4</td><td>1</td></tr>
<tr><td rowspan="3">0.05</td><td>0</td><td>0</td></tr>
<tr><td>2</td><td>1</td></tr>
<tr><td>4</td><td>2</td></tr>
<tr><td rowspan="6">0.1</td><td rowspan="2">0</td><td>0</td></tr>
<tr><td>1</td></tr>
<tr><td rowspan="3">2</td><td>0</td></tr>
<tr><td>1</td></tr>
<tr><td>2</td></tr>
<tr><td>4</td><td>1</td></tr>
<tr><td rowspan="3">0.2</td><td>0</td><td>0</td></tr>
<tr><td>2</td><td>1</td></tr>
<tr><td>4</td><td>2</td></tr>
<tr><td rowspan="6">0.4</td><td rowspan="2">0</td><td>0</td></tr>
<tr><td>1</td></tr>
<tr><td rowspan="3">2</td><td>0</td></tr>
<tr><td>1</td></tr>
<tr><td>2</td></tr>
<tr><td>6</td><td>1</td></tr>
</table>

We used Fe foil as an energy calibration to perform all the measurements in order to obtain more accurate spectra. We prepared $ZnFe_2O_4$ and Fe_xC, which are possible phases of catalysts during FTS, for XAS measurements. $ZnFe_2O_4$ was prepared by co-precipitation of zinc and iron nitrates (Zn/Fe=1/2) with ammonium carbonate (1M) at 80 ^oC at a constant pH of 7.0. Then, the precipitate was calcined in dried air at 400 ^oC for 4 h followed by at 600 ^oC for 24 h. Fe_xC was prepared by temperature-programmed reaction (10 ^oC/min) of precipitated Fe_2O_3 (0.2g) with CO (100 cm^3/min) at temperatures up to 800 ^oC. Fe_xC was passivated by flowing 1 % O_2 in He for 1 h before removing from the synthesis cell. Five samples from the University of Kentucky consisted of unpromoted precipitated Fe oxides (RJO 249) and its samples used for various lengths of time for FTS (RJO282C, D, G and J) at autoclave well mixed reactors. These samples were finely ground, fixed in a plate window, and sealed with Kapton tape. A metal roller was rolled on sealed samples to make them of the same beam path (1mm). Some samples containing high Fe content were diluted to 7~15 wt.% Fe with graphite powder in order to improve the quality of the spectra.

In addition, we measured the XAS spectra of Fe oxides during the reduction and carburization in CO and in synthesis gas. For *in-situ* Fe K-edge spectra, we diluted the samples with graphite powder in order to produce samples with 7 wt.% Fe. The samples were ground with graphite, pressed into pellets, sieved to retain the 45-60 mesh fraction, and loaded into a quartz capillary cell described in the previous quarterly report.

We measured Fe K-edge spectra on beamline IV-3 (30-100 mA at 3.0 GeV). A silicon (111) monochrometer with an unfocussed beam was used to scan the X-ray absorption spectra. To eliminate higher order harmonics X-rays, the monochromator was detuned by 80% from a 20×3 mm beam, which was defined by the slits in the station, and a 15×1.25 mm beam was allowed to pass through the samples. A Fe foil (5μm) was mounted right before the second detector in order to measure a spectrum for the energy calibration of all the samples. X-ray absorption spectra were obtained in transmission mode. Nitrogen gas was passed through the ion chamber detectors for measuring the intensities of incident (I_0) and transmitted (I_1 and I_2) X-rays.

3.3 Fe K-edge XAS Measurement for Standard Samples

3.3.1. Fe K-Edge XANES

The Fe K-edge XAS spectra of Fe_2O_3, Fe_3O_4, FeO, $ZnFe_2O_4$ and Fe_3C are shown in Figure 1.1. The spectra for all the Fe oxides show a strong absorption edge derived from the transition of *1s* electron to the continuum; the feature is referred to as the white line. Fe oxides also show a pre-edge peak below the absorption edge, which is assigned to an allowed dipole transition from a s-state to an unoccupied p-state. The XAS spectrum for Fe_xC shows a shoulder near the edge, but no white line. Figure 1.2 shows the XANES spectra of Fe oxides and Fe_xC compounds with known structure. The pre-edge peaks of Fe oxides reflect a *1s* to *3d* electronic transition, which is dipole-forbidden in centrosymmetric structures, but becomes allowed in tetrahedral or distorted octahedral structures because of p-d orbital mixing. Bulk Fe_2O_3 has a corundum structure where six

oxygen atoms form an octahedron around Fe atoms. However, the distance of Fe-O is not equivalent. Fe has four nearest O neighbors and two close O neighbors, in other words, Fe is located in distorted octahedral holes between O atoms. Therefore, the XAS near edge spectrum of Fe_2O_3 shows a pre-edge peak. Fe_3O_4 has the spinel structure with one-third Fe in tetrahedral holes and two-thirds in octahedral holes. Those Fe atoms in tetrahedral holes exhibit its characteristic pre-edge features. FeO has the rock-salt structure, but it is always deficient in Fe, so it is not in perfect octahedral holes, and thus it shows slight pre-edge feature. $ZnFe_2O_4$ is also of inverse spinel structure in which Fe is surrounded by six oxygen atoms in an octahedron. However, the Fe-O octahedron is easily distorted and some orbital mixing between d-orbital of Fe and p-orbital of oxygen atoms occurs, leading to the presence of pre-edge. The pre-edge peak decreases in the order of Fe_3O_4>Fe_2O_3>$ZnFe_2O_4$>FeO. Fe_xC has an absorption peak around the pre-edge region of Fe oxides, but shows no pre-edge feature.

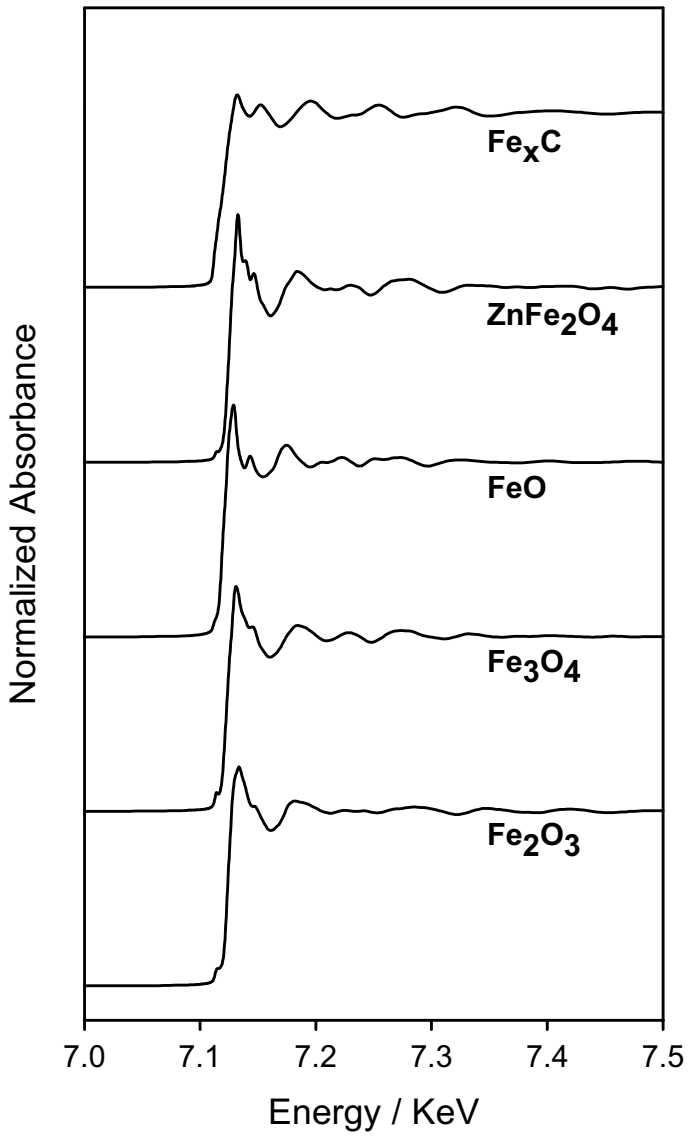

Figure 1.1. Fe K-edge XAS spectra of Fe standard compounds: Fe_2O_3, Fe_3O_4, FeO, $ZnFe_2O_4$ and Fe_xC. (Spectra measured at ambient temperature and atmospheric pressure)

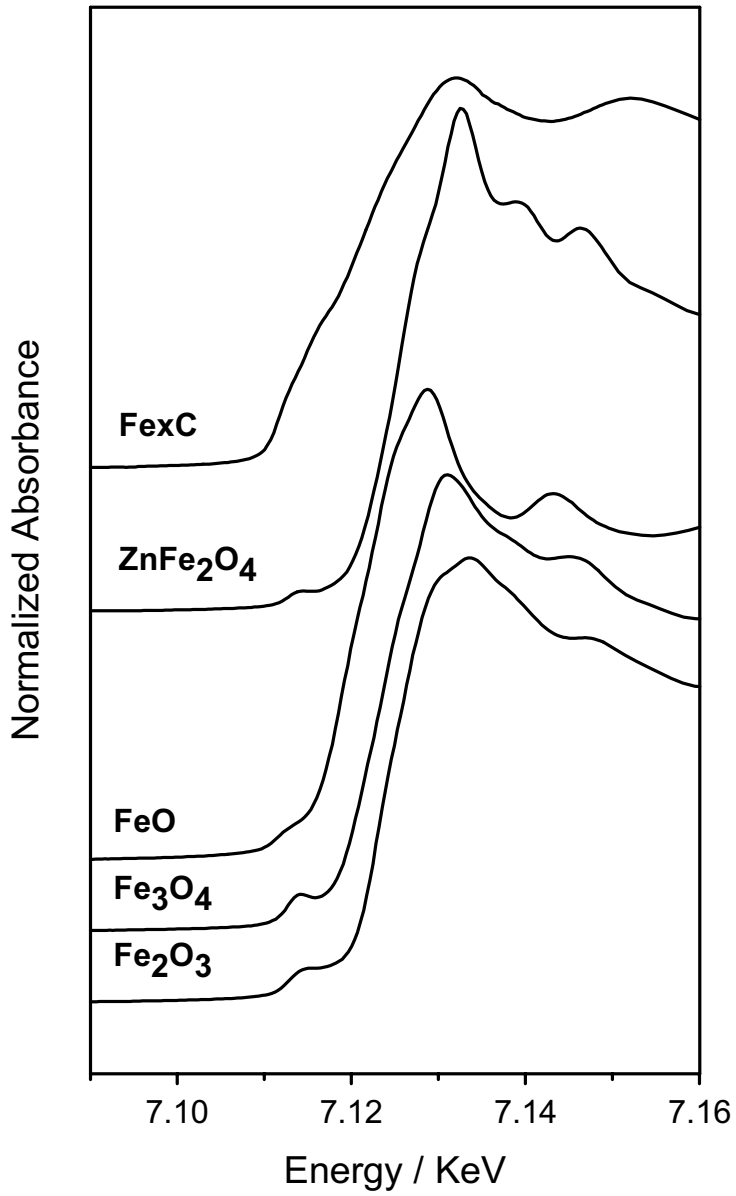

Figure 1.2. Fe K-edge XANES spectra of Fe standard compounds: Fe_2O_3, Fe_3O_4, FeO, $ZnFe_2O_4$ and Fe_xC. (Spectra measured at ambient temperature and atmospheric pressure)

3.3.2 Fe K-Edge XANES Derivatice Spectra

Figure 1.3 shows the Fe K-edge XANES derivative spectra for standard compounds Fe_2O_3, Fe_3O_4, FeO, $ZnFe_2O_4$, and Fe_xC. All the Fe oxides show a pre-edge energy at 7.113 KeV with FeO showing a slight shift of the pre-edge to lower energies. Fe_2O_3, Fe_3O_4, and FeO show Fe K-edge energies at 7.123, 7.124 and 7.119 KeV, respectively, whereas $ZnFe_2O_4$ shows the first inflection point at 7.126 KeV. Fe_xC gives a K-edge

energy at 7.112 KeV, which is the same as that of metallic Fe. We use the first inflection point beyond the pre-edge as the absorption threshold energy.

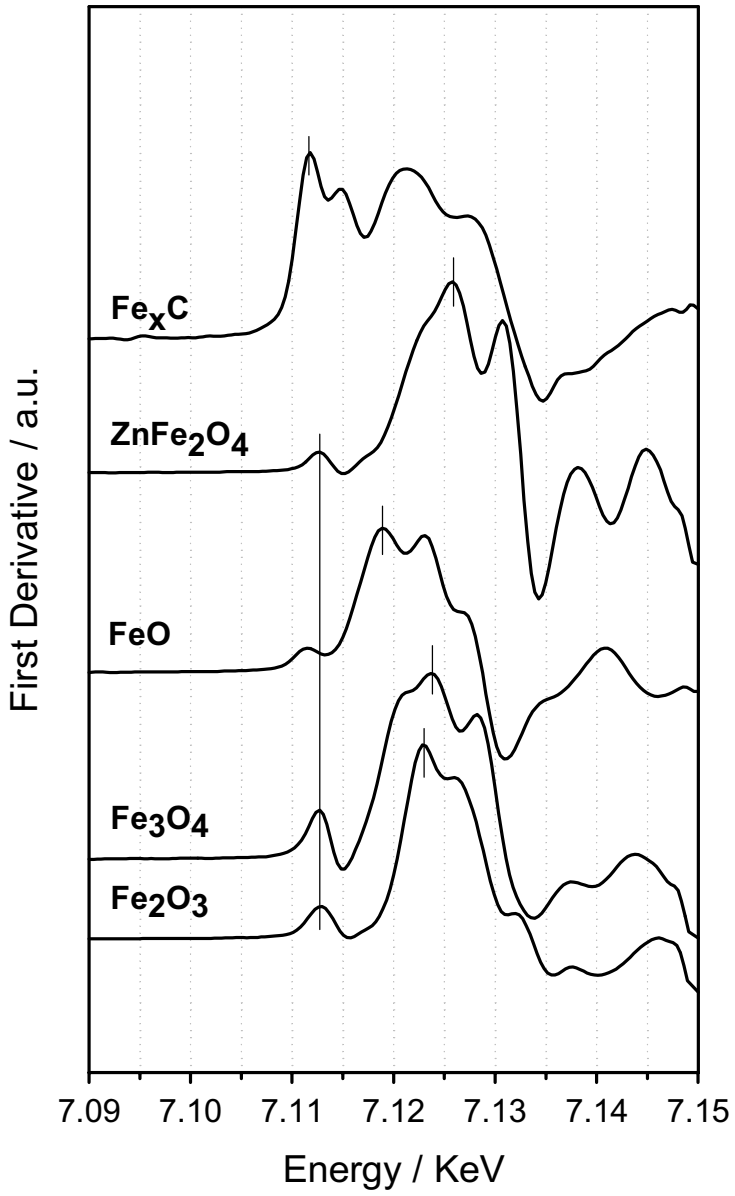

Figure 1.3. Fe K-edge XANES derivative spectra of Fe standard compounds: Fe_2O_3, Fe_3O_4, FeO, $ZnFe_2O_4$ and Fe_xC. (Spectra measured at ambient temperature and atmospheric pressure)

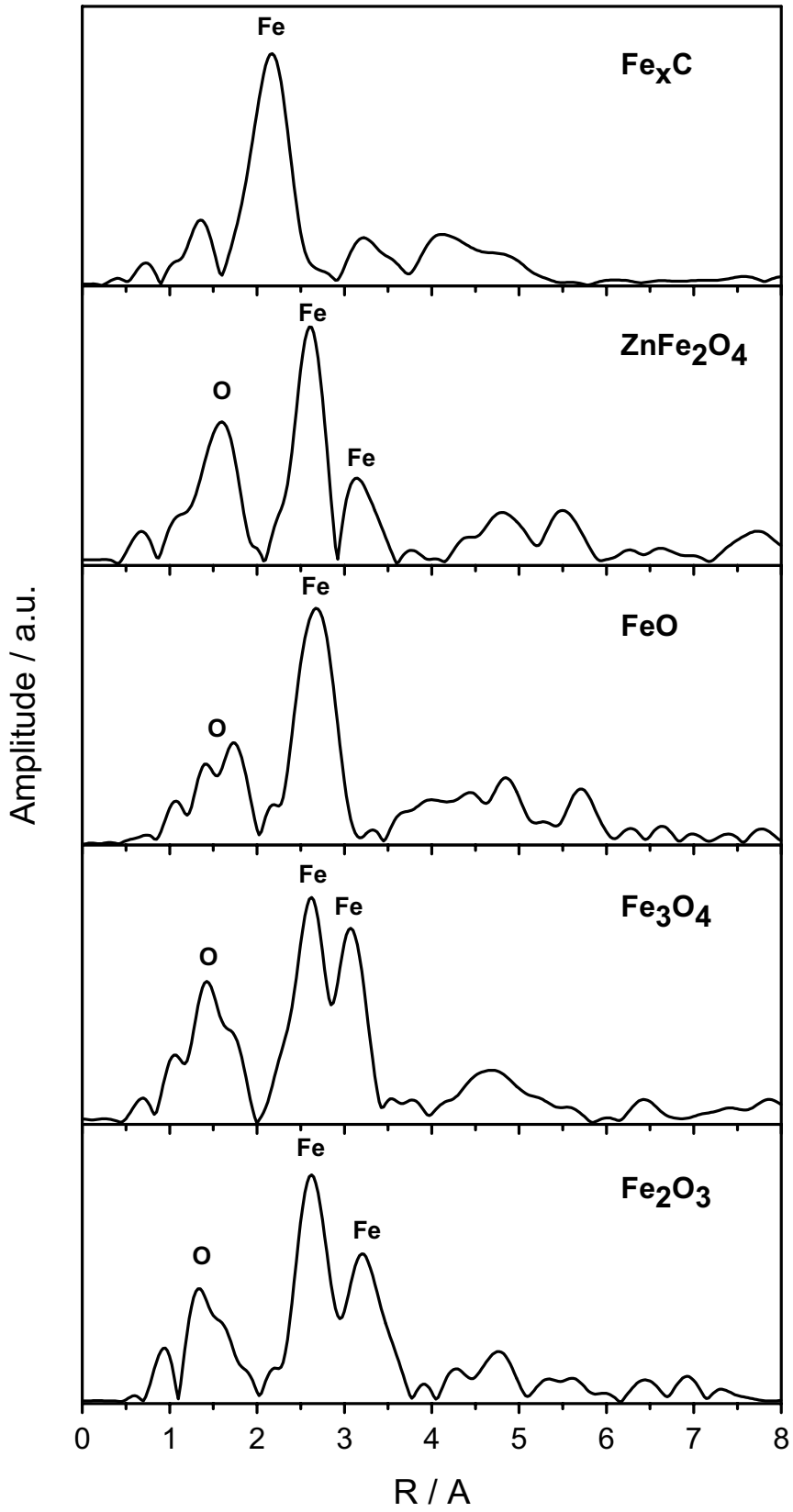

Figure 1.4. EXAFS of Fe K-edge for Fe standard compounds: Fe_2O_3, Fe_3O_4, FeO, $ZnFe_2O_4$ and Fe_xC. (Spectra measured at ambient temperature and atmospheric pressure)

3.3.3. Fe K-Edge EXAFS

Figure 1.4 shows the Fe K-edge Fourier transforms of the extended X-ray absorption fine structure (EXAFS) of standard compounds Fe_2O_3, Fe_3O_4, FeO, $ZnFe_2O_4$ and Fe_xC. k^3-weighting, which compensates for the reduction of the EXAFS oscillation in the high k-region and diminishes the effect of the edge jump and the ambiguity of E_o, is used for the analysis of EXAFS in order to emphasize the contribution of heavier atoms. For Fe_2O_3, Fe_3O_4, and $ZnFe_2O_4$, Fe is coordinated to first nearest neighbor Fe atoms at 2.6 Å and to second nearest neighbor Fe atoms at 3.2 Å for Fe_2O_3 and $ZnFe_2O_4$ and 3.1 Å for Fe_3O_4, respectively; Fe in FeO is coordinated to the first closest neighbor Fe atoms at 2.7 Å. For Fe_xC, its Fourier transform shows a Fe-Fe distance at 2.2 Å, which is the same as that of first nearest Fe neighbor atoms in Fe metal.

3.4. Fe K-edge XAS Measurement for Fe-Zn-K-Cu Oxides

3.4.1. Fe K-Edge EXAFS

In order to study the effect of the incorporation of Zn, K and Cu on the structure of Fe oxides, we also measured the Fe K-edge XAS spectra of coprecipitated Fe-Zn oxides impregnated with K and Cu. Figure 1.5 shows the Fe K-edge EXAFS Fourier transform spectra of Fe-Zn-K-Cu oxides. The EXAFS spectra of Fe-K-Cu oxide and Fe-Zn-K-Cu oxide resemble that of Fe_2O_3, except that the coordination environment of Fe by O atoms is slightly different from that of Fe_2O_3. This indicates that the crystal structure of Fe_2O_3 is mostly retained with the impregnation of K and Cu.

3.5. In-situ Fe K-edge XAS Measurement for Fe Oxides in CO and Synthesis Gas

3.5.1. Fe K-Edge EXAFS

Figure 1.6 shows the Fe K-edge EXAFS Fourier transform spectra of Fe oxides in CO (A) or in synthesis gas (C). The EXAFS spectra (A) of Fe oxide after treatment in CO at temperatures up to 700 ^oC resemble that of standard Fe_xC, indicating that FexC is formed in CO at this temperature. This observation confirmed our conclusion in the previous report that oxygen in Fe-Zn-K-Cu oxide can be removed completely at 500 ^oC in more than 4 h or higher temperature in shorter time. The Fe K-edge EXAFS spectra of Fe oxide in synthesis gas at 250 ^oC for 9 h is more complicated than in CO at 500 ^oC. Fe is mainly coordinated to oxygen atoms, and the spectra resemble that of Fe_3O_4. Also, there is small peak of Fe_xC present in the spectra. This indicates that Fe_2O_3 has been reduced and carburized to a mixture of Fe_3O_4 and Fe_xC under the reaction condition investigated.

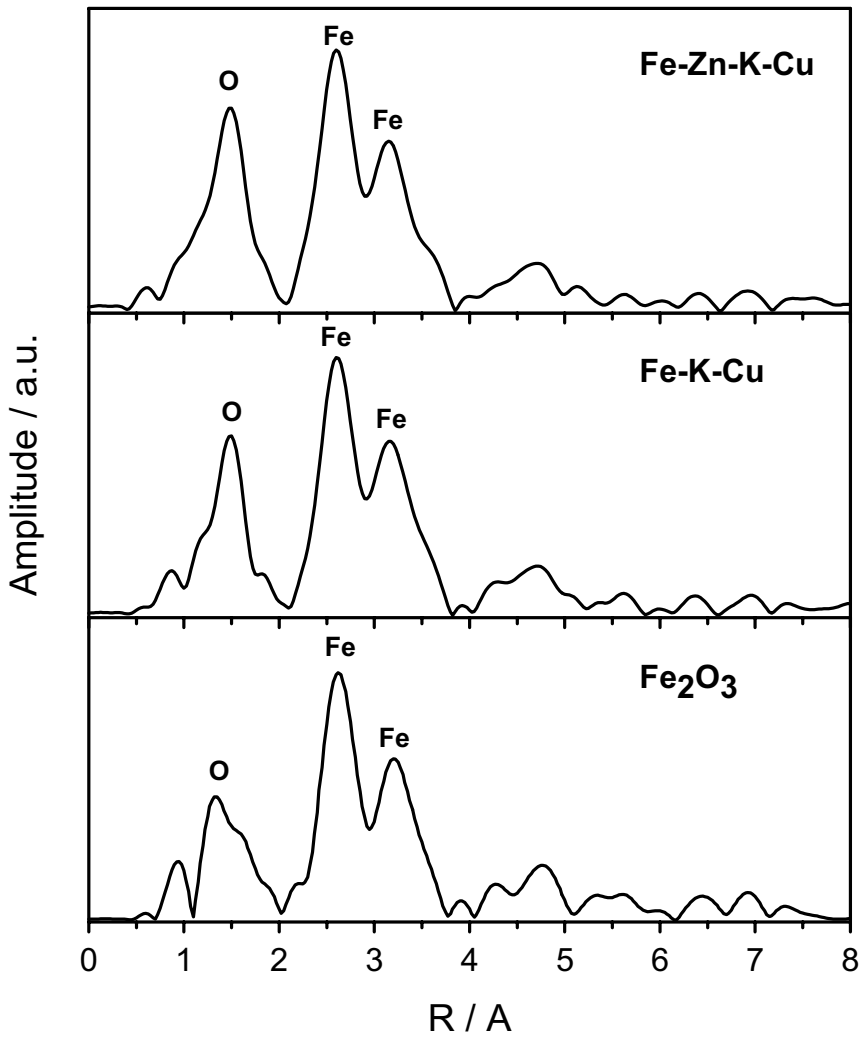

Figure 1.5. Fe-K-edge EXAFS for Fe-Zn-K-Cu oxides. (Zn/Fe=0.1, K/M=0.02, Cu/M=0.01, M=(Fe+Zn))

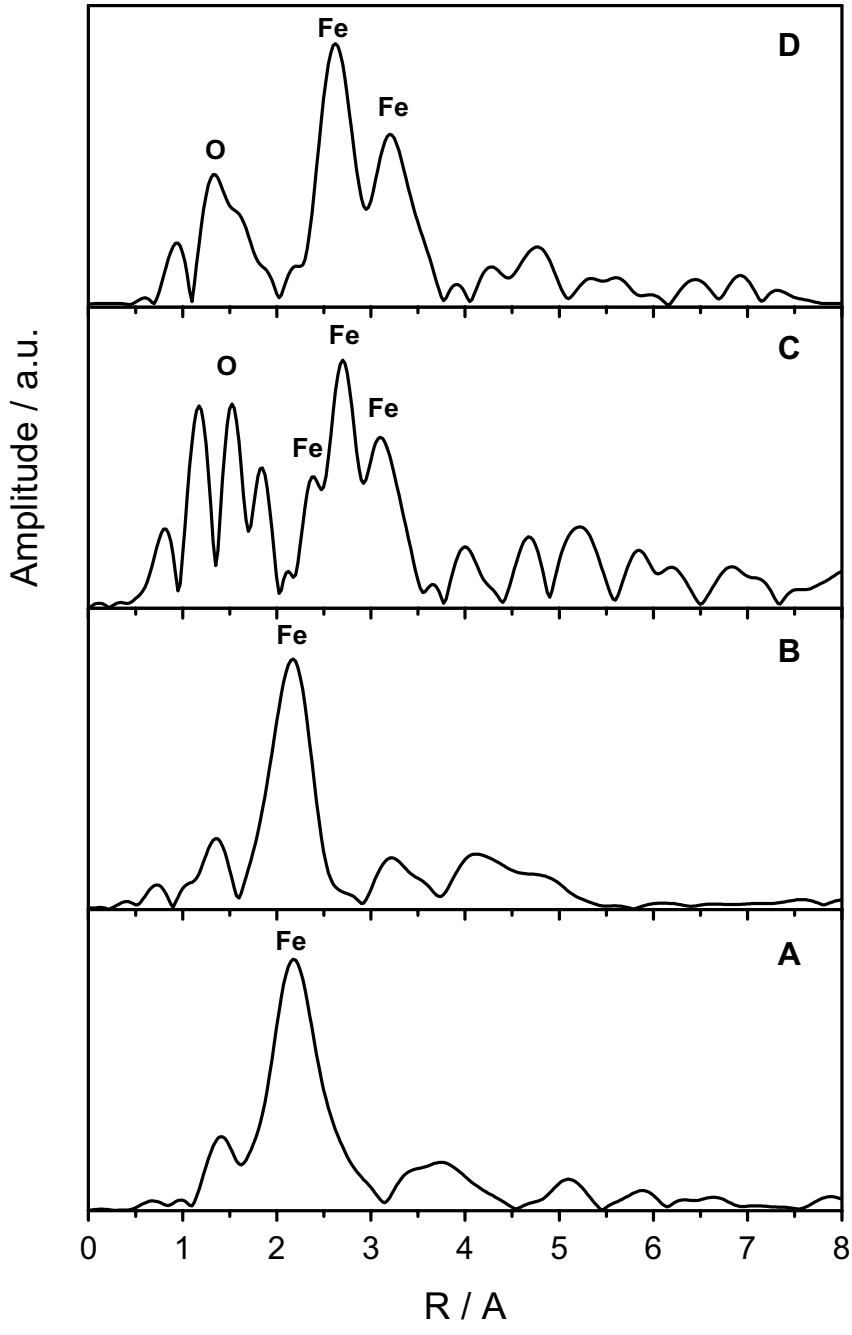

Figure 1.6. *In-situ* Fe K-edge EXAFS Fourier transform spectra. A: Fe oxide in CO at temperatures up to 700 ^{o}C (8 mg sample; 7 wt% Fe; 1.5 cm^3/min), B: Fe_xC; C: Fe oxide in CO/H_2 at 250 ^{o}C for 9 h (8 mg sample; 7 wt% Fe; CO/H_2=1/2, 1.5 cm^3/min); D: Fe_2O_3.

3.6 Fe K-edge XAS Measurement for CAER's Samples

3.6.1 Fe K-Edge XANES

Table 1.2 shows the specification of CAER's samples. RJO249 is unpromoted precipitated Fe oxide and RJO282C, D, G and J are RJO249 used for various lengths of time for FTS at autoclave well mixed reactors. The Mossbauer data provided by CAER shows that the extent of carburization increases and reaches a highest value and then decreases gradually with time on stream. After 432 h, all the carbides were converted to Fe_3O_4.

Figure 1.7 shows the normalized X-ray absorption spectra of RJO249, RJO282C, D, G and J. The smoothness of the spectra indicates that the distortion caused by imperfect monochromatization or improper sample preparation was mostly eliminated. Figure 1.8 shows the X-ray near edge structure (XANES) regions of theses samples. All the spectra present pre-edge peaks and white lines with RJO249 and RJO282G and RJO282J showing prominent features than other two samples. This indicates that more oxide species are present in samples RJO 24, RJO282G and RJO282J.

Table 1.2 Specification of CAER's samples (University of Kentucky)

Sample	RJO249	RJO282C	RJO282D	RJO282G	RJO282J
Reaction time (h)	0	71	121	264	432
Mossbauer Identification	-	70% Fe_5C_2 30% Fe_3O_4	55% Fe_5C_2 45% Fe_3O_4	25% Fe_5C_2 75% Fe_3O_4	Fe_3O_4

3.6.2 Fe K-Edge XANES Derivative Spectra

The XANES derivative spectra are shown in Figure 1.9. All the spectra show a pre-edge energy at 7.113 KeV. The energies at the first inflection point of RJO249, RJO282C, D, G and J are 7.123, 7.124, 7.124, 7.124, 7.125 KeV respectively. Compared with the threshold energy of standard compounds Fe_2O_3, Fe_3O_4, FeO and Fe_xC, which are 7.123, 7.124, 7.119, and 7.112 KeV, it is confirmed that all these samples contain significant amounts of Fe oxides. The increased pre-edge peaks of RJO282C and RJO 282D samples at 7.113 KeV suggest that this sample also contain other species, probably Fe carbides with absorption energy at 7.112 KeV.

3.6.3 Fe K-Edge EXAFS

Figure 1.10 shows the Fe K-edge EXAFS Fourier transforms of each CAER's samples. RJO249 is poorly resolved, indicating the poorly coordinated environment around the absorber. The EXAFS spectra of RJO282C and RJO282D are not well resolved either, indicating the coexistence of difference species. For RJO282C, besides the characteristic

Fe-Fe coordination of Fe_3O_4 at 3.1 Å, it shows a higher peak at 2.2 Å, which coincides with that of Fe_xC. This suggests that it contains both Fe_xC and Fe_3O_4. RJO282D contains less Fe carbide features than that of RJO282C. RJO282G shows mostly similar EXAFS features as that of Fe_3O_4, and RJO282J exhibits the same EXAFS features as that of Fe_3O_4.

3.6.4 Fe K-Edge LC XANES FIT

Table 1.3 shows the linear combination X-ray near edge spectroscopy (LC XANES) fit results of CAER's samples. Figure 1.11 shows the spectrum of RJO282D and its LC XANES fit. The small fit residual (0.8) indicates that they match very well. The LC XANES fit indicates that RJO282C, D and G contain Fe carbides and Fe_3O_4, and RJO 282J contains Fe_3O_4 alone. Although the absolute values of the contents of Fe carbide and Fe_3O_4 in the samples obtained from LC XANES are slightly different from those of Mossbauer spectrascopic measurement, their values show a consistent trend that the extent of carburization increases and reaches a highest value and then decreases gradually with time on stream. After 432 h, all the Fe carbides were converted to Fe_3O_4.

Table 1.3 Fe K-edge LC XANES fit of CAER's samples

Sample	RJO249	RJO282C	RJO282D	RJO282G	RJO282J
LC XANES Fit	-	52% FexC 48% Fe_3O_4	35% FexC 65% Fe_3O_4	2% FexC 98% Fe_3O_4	Fe_3O_4
Fit Residual	-	0.5	0.5	0.8	0.8

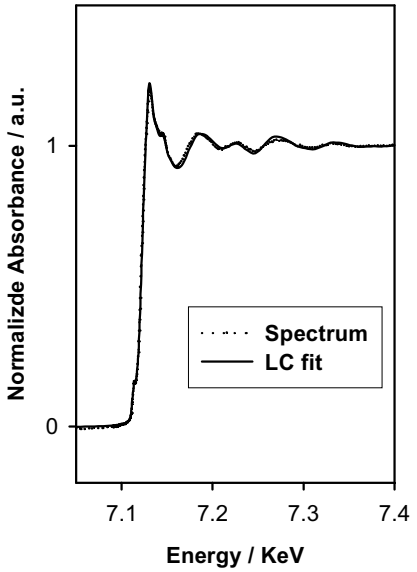

Figure 1.11. LC XANES fit of RJO282D

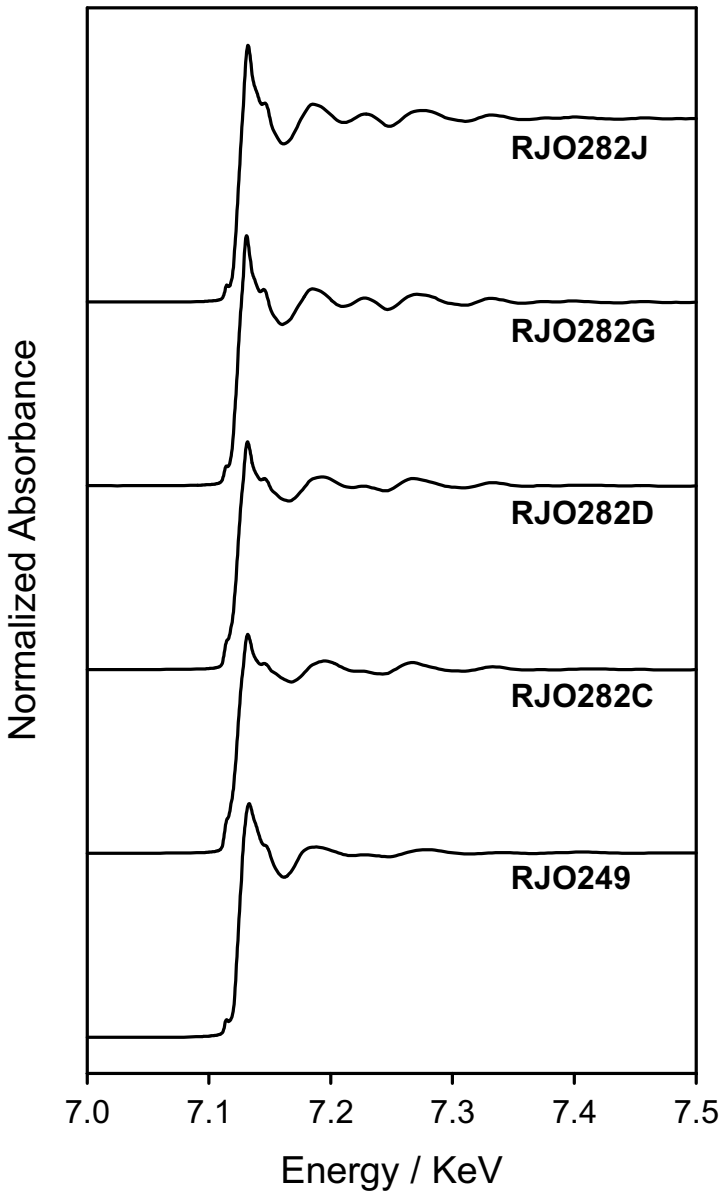

Figure 1.7 Fe K-edge XAS spectra of RJO249, RJO282C, D, G, J.
(Spectra measured at ambient temperature and atmospheric pressure)

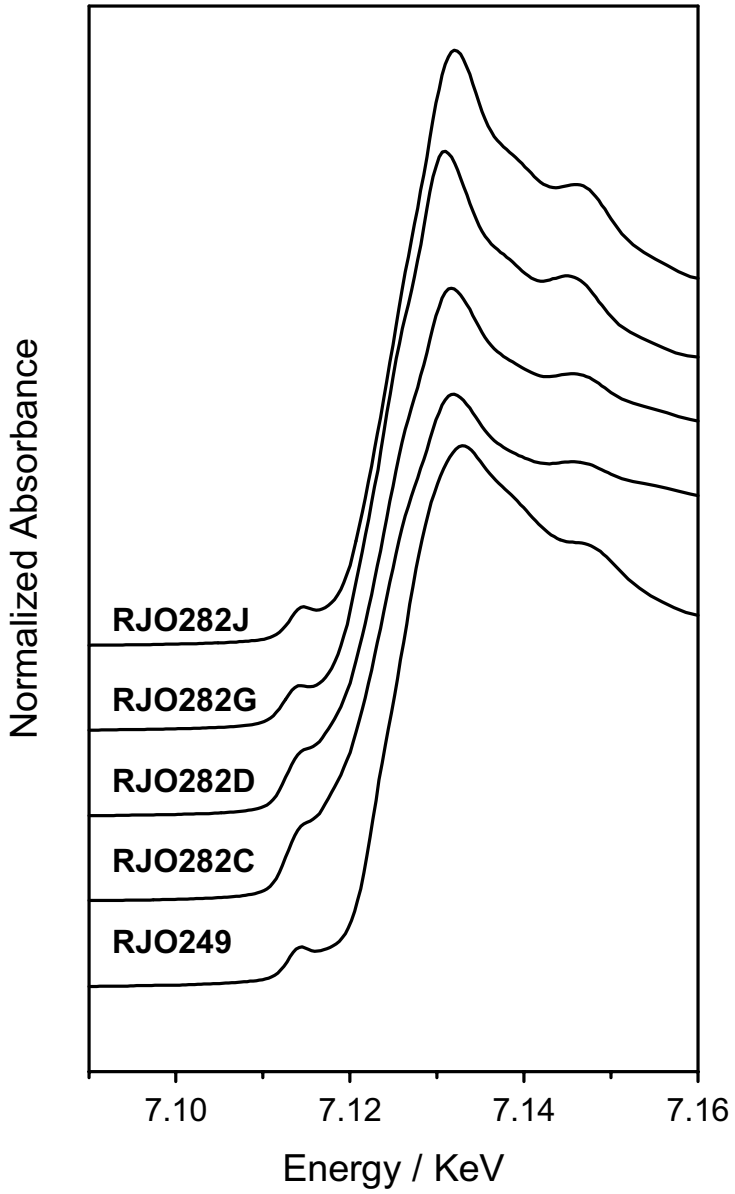

Figure 1.8

Figure 1.8 Normalized Fe K-edge XANES spectra of RJO249, RJO282C, D, G, J. (Spectra measured at ambient temperature and atmospheric pressure)

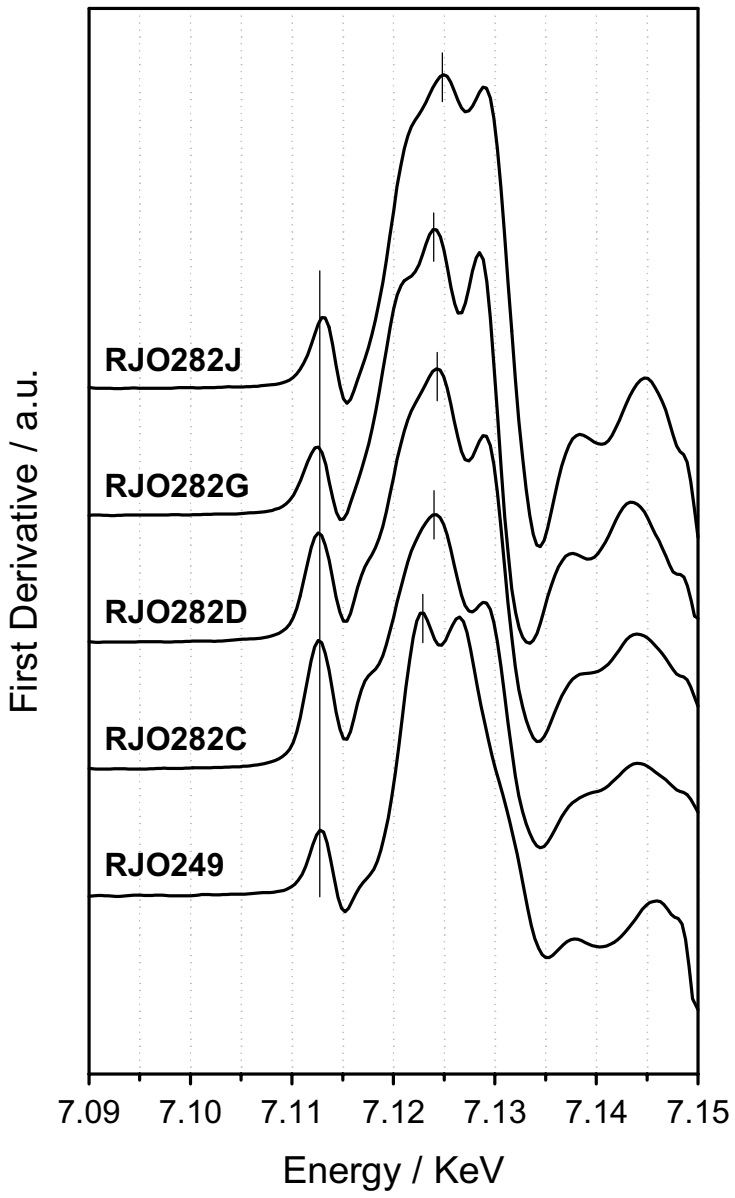

Figure 1.7 Fe K-edge XANES derivative spectra of RJO249, RJO282C, D, G, J. (Spectra measured at ambient temperature and atmospheric pressure)

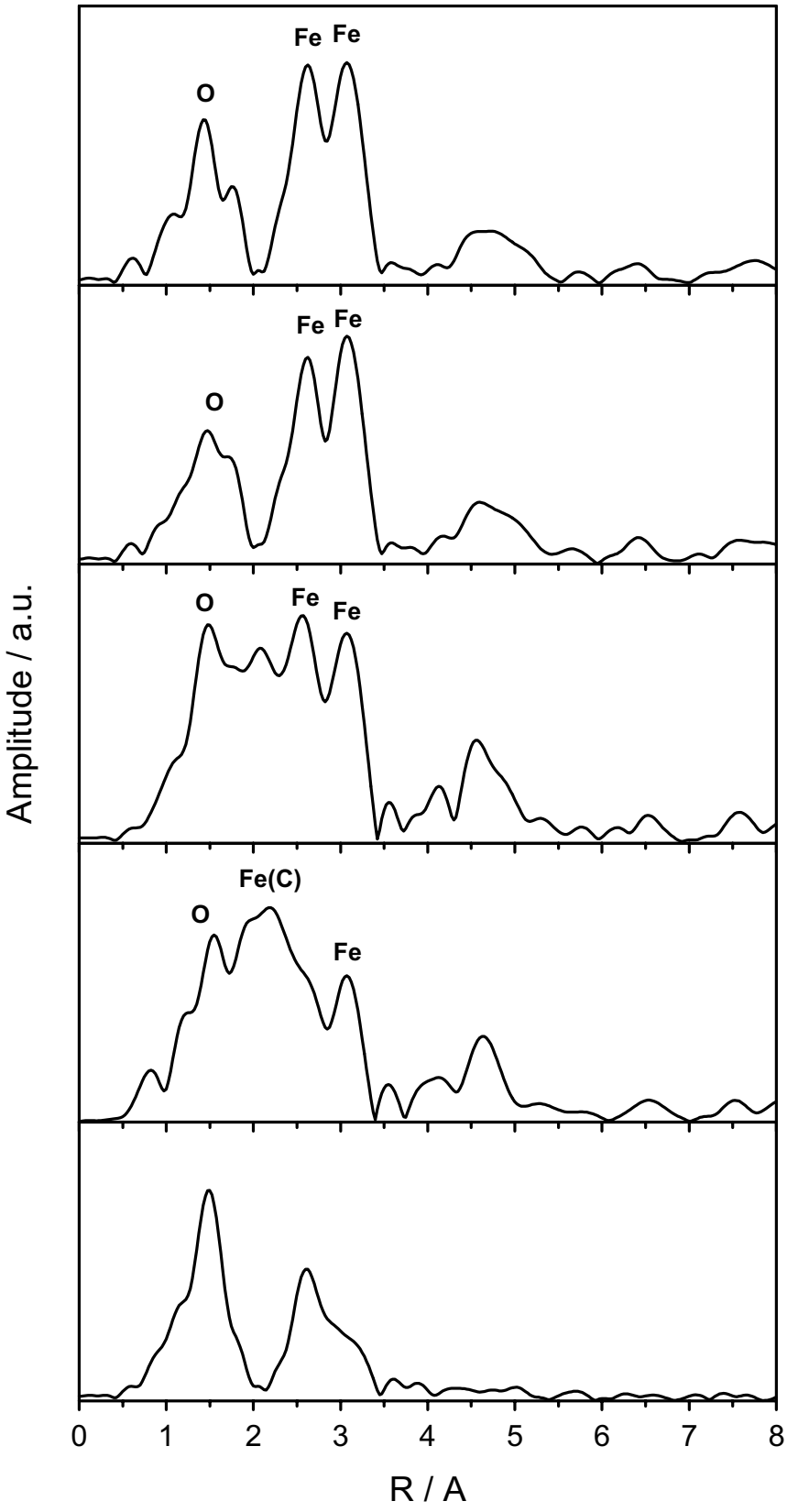

Figure 1.10 Fourier transforms of Fe K-edge EXAFS of RJO249, RJO282C, D, G, J. (Spectra measured at ambient temperature and atmospheric pressure)

4. Fischer-Tropsch synthesis on Fe-based catalysts

4.1. Investigation of H_2/D_2 Isotope Effects on FTS Reactions

During this reporting period, H_2/D_2 kinetic isotope effects (KIE) were investigated on FTS reactions over the Fe-based catalyst (Zn/Fe=0.1, K/M=0.02, Cu/M=0.01) at various space velocities in a fixed-bed reactor at 235 ^oC and 21.4 atm using synthesis gas with a H_2/CO or D_2/CO ratio of 2:1.

4.1.1 H_2/D_2 Effects of FTS Reaction Rates

Figs. 1.12-1.14 show CO conversion rates and hydrocarbon and CO_2 formation rates as a function of CO conversion on the catalyst (Zn/Fe=0.1, K/M=0.02, Cu/M=0.01) at 235 ^oC and 21.4 atm. CO conversion and hydrocarbon formation rates were much higher with D_2/CO than with H_2/CO mixture. In contrast, CO_2 formation rate was lower with D_2/CO than with H_2/CO. It has been proposed that the formation of higher molecular weight hydrocarbons on Fe-based catalyst during FTS reactions is initiated by the addition of a methyl group to a methylene group and that further chain growth occurs by the reaction of methylene group with adsorbed alkyl groups. The alkyl groups then react to form olefins and paraffins via either hydrogen elimination or addition. Consistent with these views of CO hydrogenation, one would expect to observe a normal isotopic effect if D_2 were used instead of H_2.

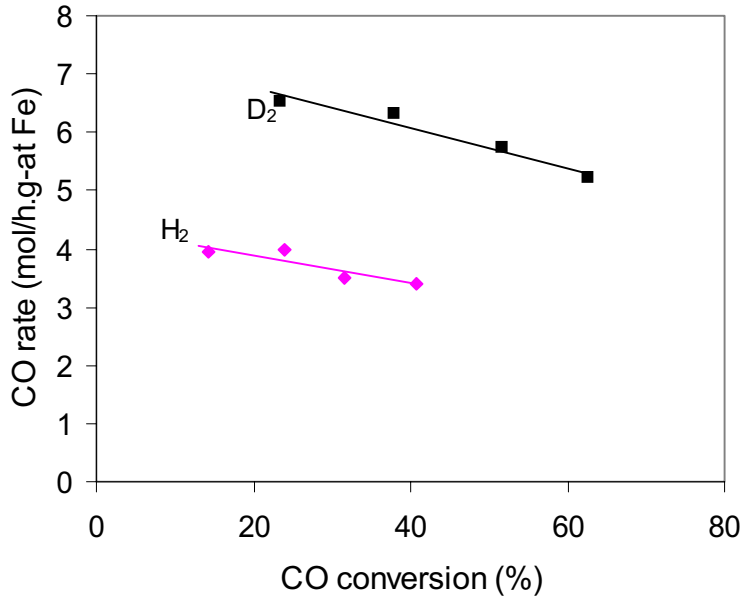

Fig.1.12 CO conversion rate as a function of CO conversion for H_2/CO or D_2/CO reactants (Zn/Fe=0.1, K/M=0.02, Cu/M=0.01) at 235 ^oC and 21.4 atm.

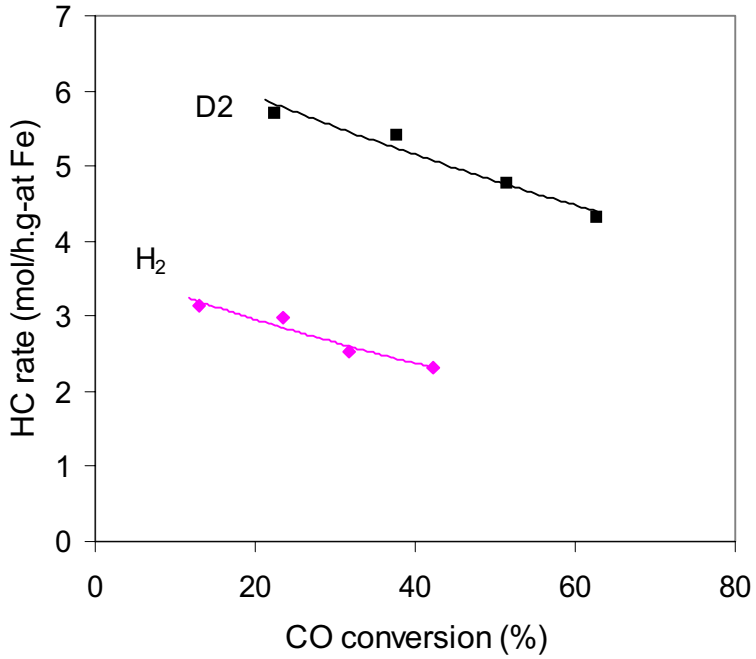

Fig.1.13 Hydrocarbon formation rate as a function of CO conversion for H_2/CO or D_2/CO reactants (Zn/Fe=0.1, K/M=0.02, Cu/M=0.01) at 235 ^oC and 21.4 atm.

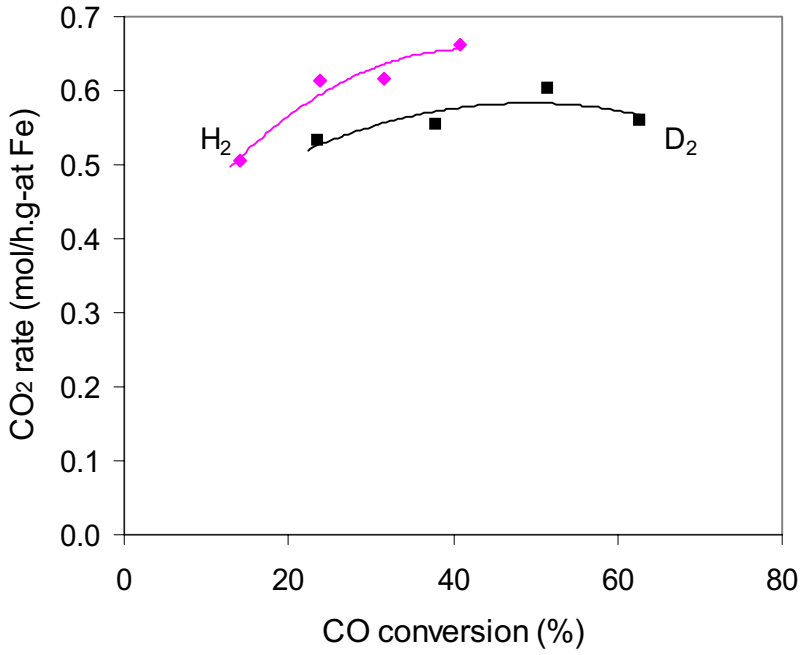

Fig.1.14 CO_2 conversion rate as a function of CO conversion for H_2/CO or D_2/CO reactants (Zn/Fe=0.1, K/M=0.02, Cu/M=0.01) at 235 ^oC and 21.4 atm.

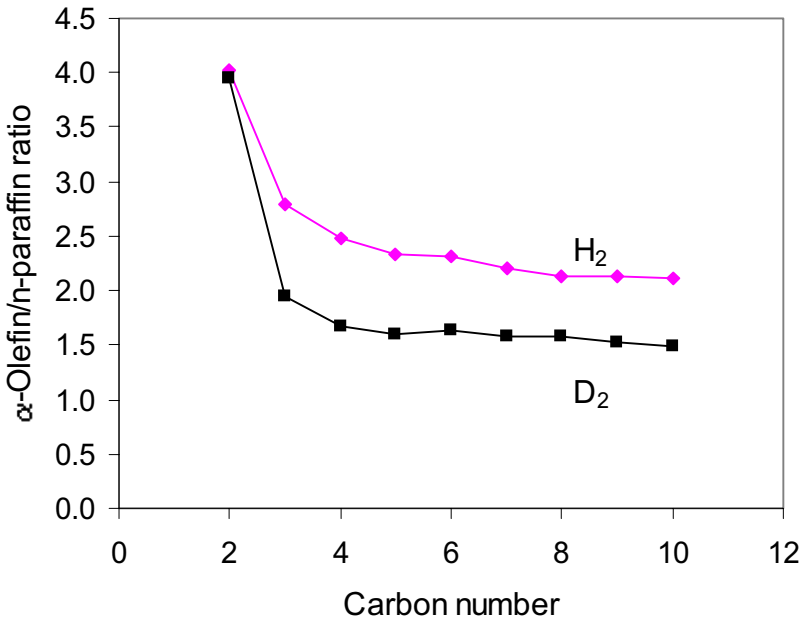

Fig.1.15 α-Olefin/n-paraffin ratio as a function of CO conversion for H_2/CO or D_2/CO reactants (Zn/Fe=0.1, K/M=0.02, Cu/M=0.01) at 235 °C and 21.4 atm.

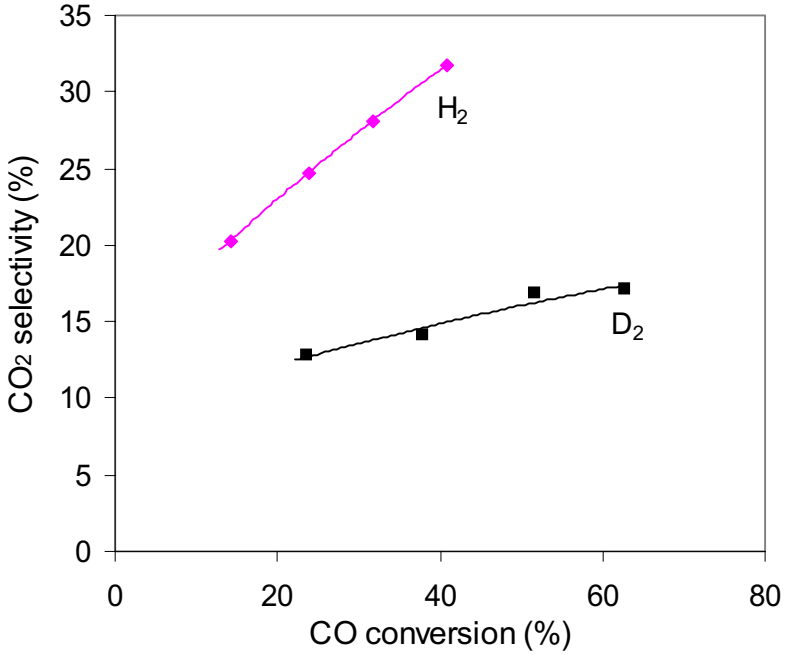

Fig.1.16 CO_2 selectivity as a function of CO conversion for H_2/CO or D_2/CO reactants (Zn/Fe=0.1, K/M=0.02, Cu/M=0.01) at 235 °C and 21.4 atm.

However, we observed an inverse isotopic effect as D_2 was used instead of H_2. Wilson [21] noted that the overall isotopic effect for CO hydrogenation could arise from a combination of kinetic and equilibrium isotope effects, the former favoring the reaction

of H_2 and the latter favoring the reaction of D_2. The inverse isotopic effects of our observations suggested a dominant role of the thermodynamic effects. The higher CO conversion and hydrocarbon formation rates may reflect the stronger adsorption of D_2 than that of H_2 on the Fe-based catalyst. Fig. 1.15 shows α-olefin/n-paraffin ratio as a function of carbon number. Fig. 1.16 shows CO_2 selectivity as a function of CO conversion. The increase in surface H_2 or D_2 concentration on the catalyst increases the probability of hydrogen addition of the adsorbed alkyl to form paraffins and decrease the probability of hydrogen elimination of the adsorbed alkyl to form olefins. The increase in surface H_2 or D_2 concentration also decreases the formation of CO_2 via water-gas shift reaction by causing the removal of the oxygen in CO by adsorbed hydrogen rather than adsorbed CO. Hence, both lower α-olefin/n-paraffin ratio with D_2 as shown in Fig. 1.15 and lower CO_2 selectivity with D_2 as shown in Fig. 1.16 suggest that higher surface concentrations of H isotopes are present when D_2 is used. The higher surface D_2 concentration is due to its larger adsorption equilibrium coefficient. This result is in agreement with previous studies. Soller [22] observed about 1.4 times more adsorption of D_2 than H_2 on Cu powder at 125 ^oC. Larger adsorption coefficients were obtained for D_2 than for H_2 on Ni during the hydrogenation of acetylene [23] and of CO_2 [24].

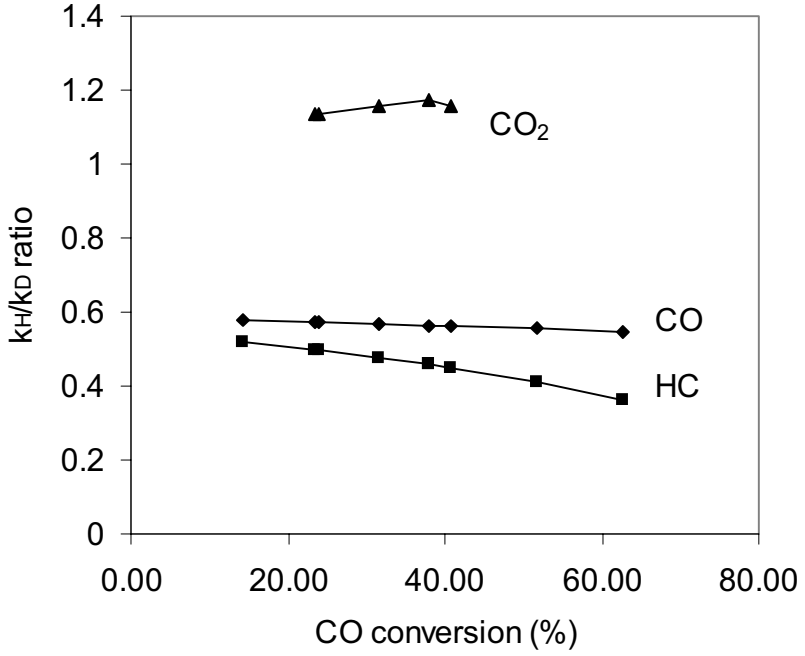

Fig.1.17 k_H/k_D ratio for CO conversion, hydrocarbon and CO_2 formation as a function of CO conversion for H_2/CO or D_2/CO reactants (Zn/Fe=0.1, K/M=0.02, Cu/M=0.01) at 235 ^oC and 21.4 atm.

A reaction rate expression proposed [25] for FTS is

$$-r_{CO+H_2} = \frac{kP_{CO}P_{H_2}^2}{P_{CO}P_{H_2} + bP_{H_2O}}$$

Where b is adsorption parameter and k is rate constant. Based on this rate expression, hydrocarbon formation rate ($-r_{CO+H_2}$) almost linearly increase with hydrogen pressure at low conversion. Since FTS reactions proceed on the surface of the catalyst and surface hydrogen concentration is determined by hydrogen pressure, higher surface hydrogen concentration gave higher hydrocarbon formation rate. Therefore, CO conversion and hydrocarbon formation rates were higher with D_2 at same CO conversion, as shown in Figs. 1.12 and 1.13. Likely, a lower CO_2 formation rate as shown in Fig. 1.14 was also due to the higher surface deuterium concentration since hydrogen is one of products of water-gas shift reaction.

4.1.2 k_H/k_D Ratio

The isotopic effect can be expressed by a ratio of k_H/k_D. k_H and k_D are rate constants for H_2 and D_2, respectively. Since we did not have experimental value for both k_H and k_D at the same CO conversion, we got k_H values by fitting the curve of rate vs. CO conversion for experimental values of k_D and also get a fitted value of k_D for each experimental value of k_H by a similar way.

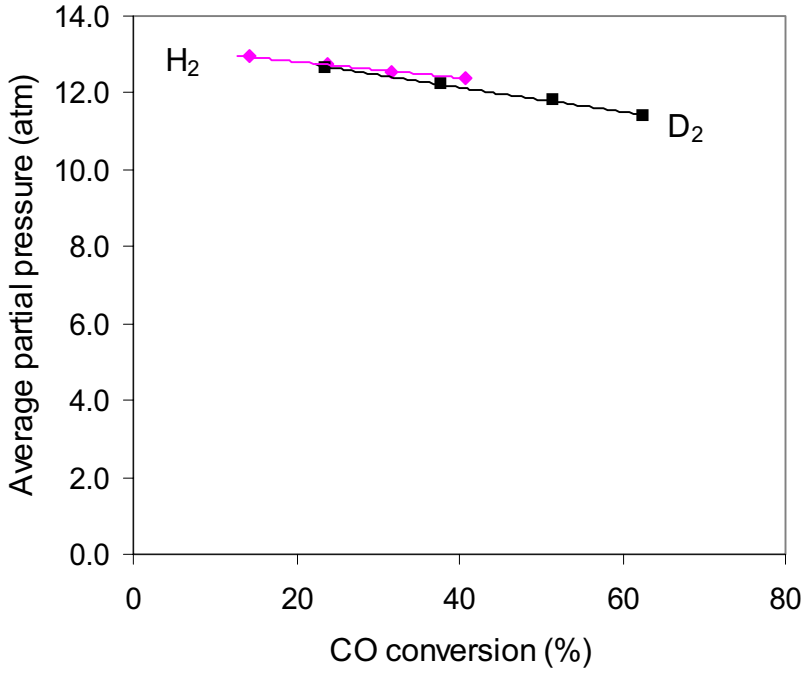

Fig.1.18 Average partial pressure of hydrogen as a function of CO conversion for H_2/CO or D_2/CO reactants (Zn/Fe=0.1, K/M=0.02, Cu/M=0.01) at 235 ^oC and 21.4 atm.

Fig. 1.17 shows k_H/k_D ratio for CO conversion, hydrocarbon and CO_2 formation as a function of CO conversion. The k_H/k_D ratio for hydrocarbon formation was about 0.5 and slightly decrease with increasing CO conversion. The k_H/k_D ratio for CO_2 formation was greater than 1. The inverse isotopic effect for hydrocarbon formation (k_H/k_D <1) and the normal isotopic effect for CO_2 formation (k_H/k_D > 1) are expected because higher surface hydrogen concentration was present when D_2 was used. It is not clear why the k_H/k_D ratio for hydrocarbon formation decreased with increasing CO conversion. The reason might be that the partial pressure of hydrogen changes with CO conversion. Fig. 1.18 shows the partial pressure of hydrogen as a function of CO conversion. It is seen that the partial pressures for both H_2 and D_2 decreased with increasing CO conversion. We speculate that surface hydrogen concentration is more sensitive to the reduction of pressure in gas phase for H_2 than that for D_2 because the adsorption coefficient of D_2 is higher than that of H_2. Accordingly, hydrocarbon formation rate decreased faster with decreasing partial pressure for H_2 than for D_2. Hence, the k_H/k_D ratio for hydrocarbon formation decreased with increasing CO conversion (Fig. 1.17).

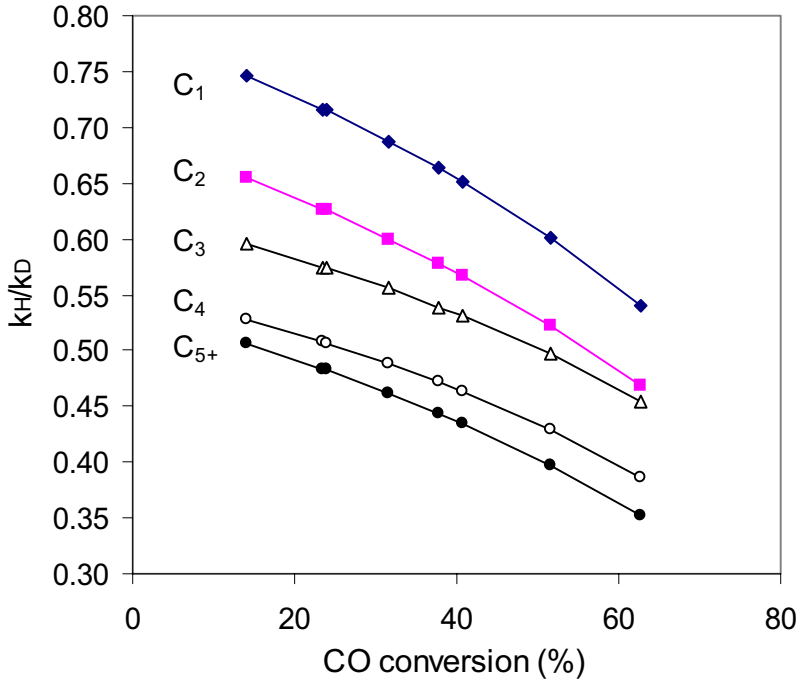

Fig.1.19 k_H/k_D ratios for C_1-C_4 and C_{5+} as a function of CO conversion for H_2/CO or D_2/CO reactants (Zn/Fe=0.1, K/M=0.02, Cu/M=0.01) at 235 ^oC and 21.4 atm.

Fig. 1.19 shows the k_H/k_D ratios of C_1-C_4 and C_{5+} formation as a function of CO conversion. Similarly, all ratios decreased with increasing CO conversion. It is also seen that at the same CO conversion k_H/k_D ratio systematically decreased with carbon number, suggesting that the inverse isotopic effects are more evident for larger hydrocarbons. Deuterium appears to favor the formation of hydrocarbon with higher molecular weight because the selectivity to C_{5+} was higher when D_2 was used (Fig. 1.20). Hence, the k_H/k_D ratio decreased with carbon number.

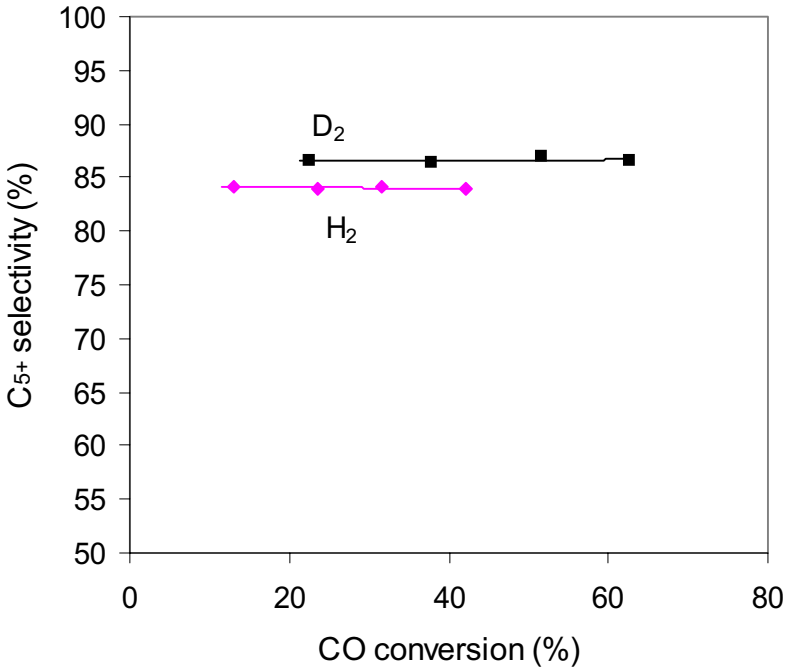

Fig.1.20 C_{5+} selectivity as a function of CO conversion for H_2/CO or D_2/CO reactants (Zn/Fe=0.1, K/M=0.02, Cu/M=0.01) at 235 ^{o}C and 21.4 atm.

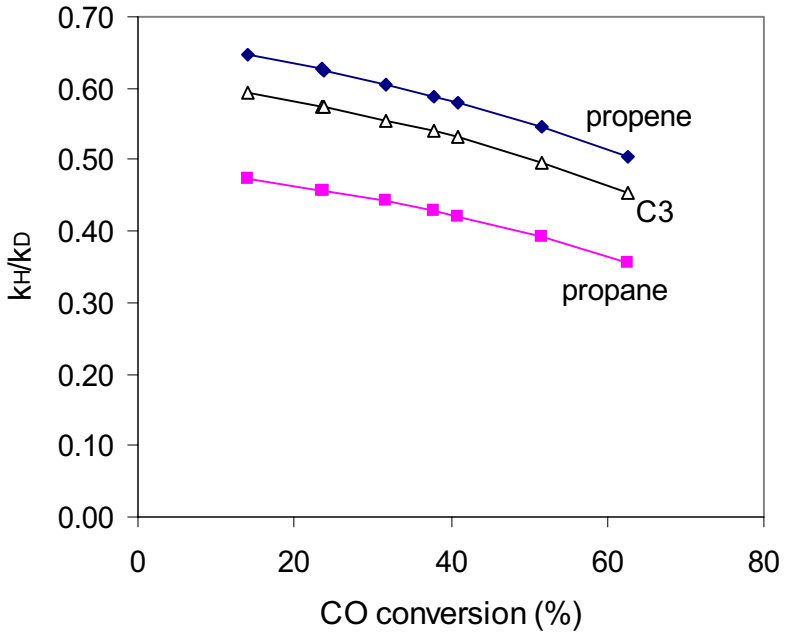

Fig.1.21 The k_H/k_D ratios of propene, propane and total C_3 as a function of CO conversion for H_2/CO or D_2/CO reactants (Zn/Fe=0.1, K/M=0.02, Cu/M=0.01) at 235 ^{o}C and 21.4 atm.

.

The isotopic effect for propene and propane is given in Fig. 1.21. The k_H/k_D ratio for propylene was higher than that for propane. Similar result was obtained for butene and butane (Fig. 1.22), suggesting that the inverse isotopic effect is more evident for paraffins than for olefins. This is because the probability of paraffin formation increased due to higher surface hydrogen concentration when D_2 was used.

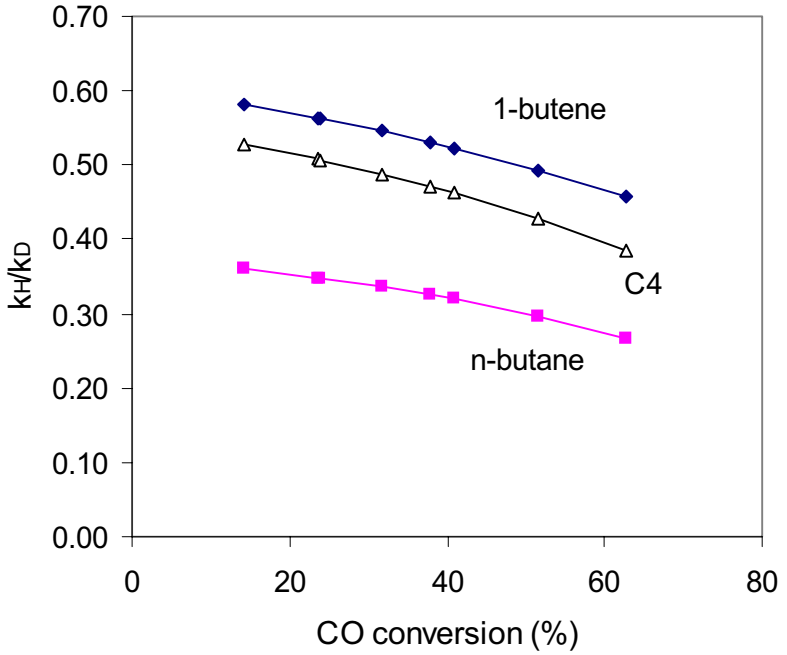

Fig.1.22 The k_H/k_D ratios of 1-butene, n-butane and total C_4 as a function of CO conversion for H_2/CO or D_2/CO reactants (Zn/Fe=0.1, K/M=0.02, Cu/M=0.01) at 235 ^oC and 21.4 atm.

.

II. FISCHER-TROPSCH SYNTHESIS ON COBALT CATALYSTS

1. Background

During last reporting period, D_2O tracer and D_2-H_2 exchange experiments were carried out during FTS. The results showed that the H_2 dissociation was quasi-equilibrated and that water dissociation was largely irreversible during FTS on Co-based catalysts. According to these findings, we proposed water-enhanced propagation in order to explain the enhancement of the synthesis rate by water observed on cobalt catalysts. During this reporting period, an additional reaction pathway was proposed for the Co-catalyzed FTS. We continued the studies of FTS reaction kinetics with focus on the effects of H_2, CO and H_2O partial pressure on FTS rate and selectivity. In addition, we conpleted the data analysis of the previous isotope effect run using H_2 and/or D_2 and obtained the kinetic isotope effects for individual hydrocarbons.

2. Experimental

FTS kinetics was studied using a fixed-bed, single-pass flow reactor. The reactants, H_2 (Matheson, UHP) and CO/N_2 (Matheson, UHP, 81.5/18.5, molar ratio) were introduced into the reactor separately using mass flow controllers (Brooks, model 5850). De-ionized water was added to the reactant feed using a high-pressure syringe pump (Isco, Inc., Model 500D). The cobalt catalyst used was a 21.9 wt% Co/SiO_2 catalyst. The preparation and pretreatment of the cobalt catalyst were described in the previous quarterly report. The reactor was kept at 20 atm, 200°C and $H_2/CO = 2.0$ for the first 100 h in order to allow the catalyst to achieve steady-state operation. The conversion of CO was varied from 5 to 30% by changing the space velocity. N_2 (used as an internal standard), CO, CO_2, and light hydrocarbons (C_1-C_{12}) were analyzed by on-line gas chromatography (Hewlett-Packard 5890) using thermal conductivity and flame ionization detections. Synthesis rate was reported as a site-time yield (molar CO converted per g atom surface Co). H_2/D_2 isotope effects were examined by comparing the rates of FTS using $H_2/CO/N_2$ (62/31/7) and $D_2/CO/N_2$ (62/31/7), which were running at 20 atm, 200°C.

3. FTS on Cobalt-base Catalysts

3.1 H_2/D_2 Isotope Effects

According to the carbide mechanism, FTS proceeds via H_2 dissociation and then stepwise hydrogenation of adsorbed carbon to form methylene monomers. The formation of higher molecular weight hydrocarbons is initiated by the addition of a methylene monomer to a methyl group. Further chain growth occurs by the reaction of methylene monomers with adsorbed alkyl groups. The alkyl groups then react to form olefins and paraffins via either hydrogen elimination or addition [26,27]. Consistent with these views of CO hydrogenation, one would expect to observe an isotopic effect if D_2 is used instead of H_2 in FTS. Such studies with H_2/D_2 may give a better understanding of FTS

reaction mechanism. However, the results available in literature have led to contradictory conclusions [28-31], probably due to a wide variations in operating conditions. In this study, H_2/D_2 isotope effects were examined under realistic FTS conditions favoring high chain growth probability (20 atm, 200°C and $H_2/CO = 2.0$).

The rate of CO consumption is presented in Figure 2.1 as a function of CO conversion. In this study, CO conversion was increased by decreasing space velocity while maintaining all other conditions. Comparing the rate obtained using H_2/CO with that for D_2/CO, we obtained a series of isotope effects (k_H/k_D) for overall CO consumption at several conversions (Figure 2.2). The data presented in Figure 2.1 show that the synthesis rate increased with the increasing CO conversion using either H_2 or D_2. In the previous report, the phenomenon was attributed to the effect of the water produced during FTS. As seen in Figure 2.2, however, the isotope effect (k_H/k_D) for CO consumption is about 0.8, independent of the CO conversion. This value is very close to that reported by Sakharov and Dokukina [28].

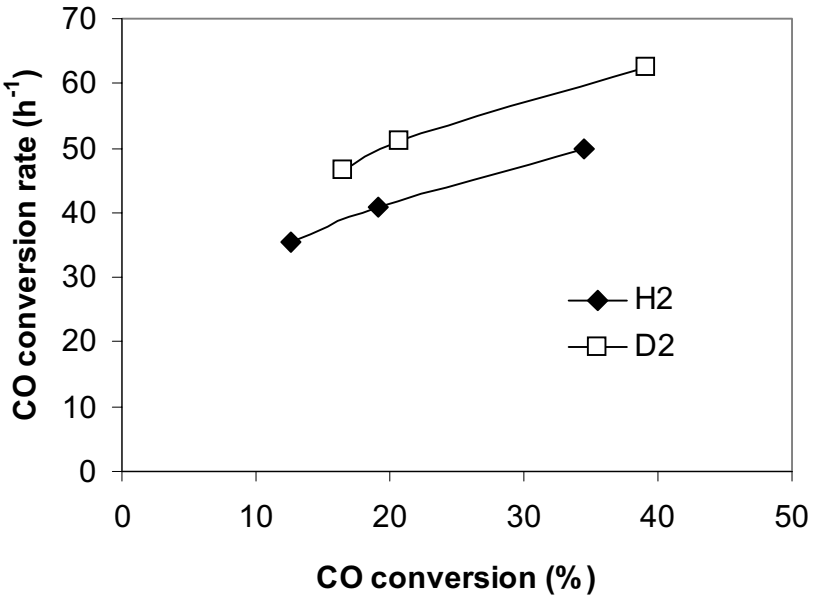

Figure 2.1. Rate of CO consumption versus CO conversion (21.9 wt% Co/SiO_2, 200°C, 20 atm, H_2/CO or $D_2/CO = 2.0$)

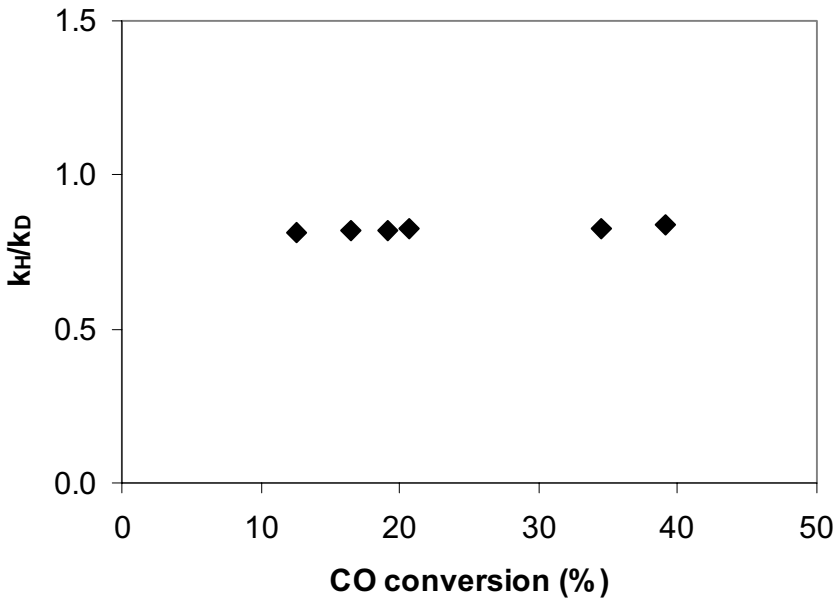

Figure 2.2. Isotope effect for CO consumption versus CO conversion (21.9 wt% Co/SiO_2, 200°C, 20 atm, H_2/CO or D_2/CO = 2.0)

Kinetic isotope effects for each hydrocarbon (C_1-C_7) were also calculated and they are shown in Figures 2.3 to 2.9. Unlike the isotope effect for CO consumption, these effects (k_H/k_D) for individual hydrocarbons change with CO conversion. In general, the effects for paraffins increase with increasing CO conversion, whereas the effects for olefins decrease with increasing CO conversion. This is not surprising when we look at the original rate data shown in Figures 2.10 to 2.16. For example, as seen in Figure 2.15, the C_6H_{12} formation rate decreases slightly with increasing CO conversion, compared to a small increase in C_6D_{12} rate. C_6H_{14} and C_6D_{14} formation rates both increase with increasing CO conversion, but the increase of the C_6D_{14} rate is not as pronounced as for the C_6H_{14} rate. These results suggest that C_nH_{2n} olefins are more reactive in secondary hydrogenation than the corresponding deuterated ones. As a result, the isotope effects (k_H/k_D) for the paraffins increased while those for the olefins decreased with increasing CO conversion.

In order to rule out the interference of secondary reactions, the lines shown in Figures 2.3 to 2.9 were extrapolated to zero conversion. Thus, isotope effects (k_H/k_D) for the paraffins (C_2-C_7) were between 0.7 and 0.9 and for methane was about 1.0. Meanwhile, normal isotope effects (around 1.1) were obtained for the olefins (C_2-C_7). Our results are somewhat different from those reported by Kellner and Bell [31]. They reported an inverse isotope effect (k_H/k_D = 0.9) for methane formation and no systematic effect for higher hydrocarbons on a Ru/SiO_2 catalyst (10 atm, < 1.5% conversion).

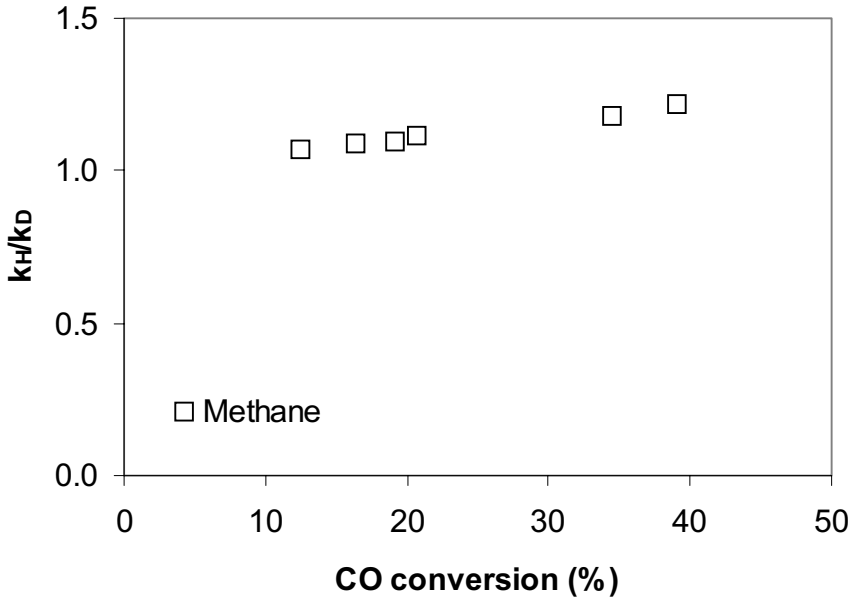

Figure 2.3. Isotope effect for methane versus CO conversion (21.9 wt% Co/SiO_2, 200°C, 20 atm, H_2/CO or D_2/CO = 2.0)

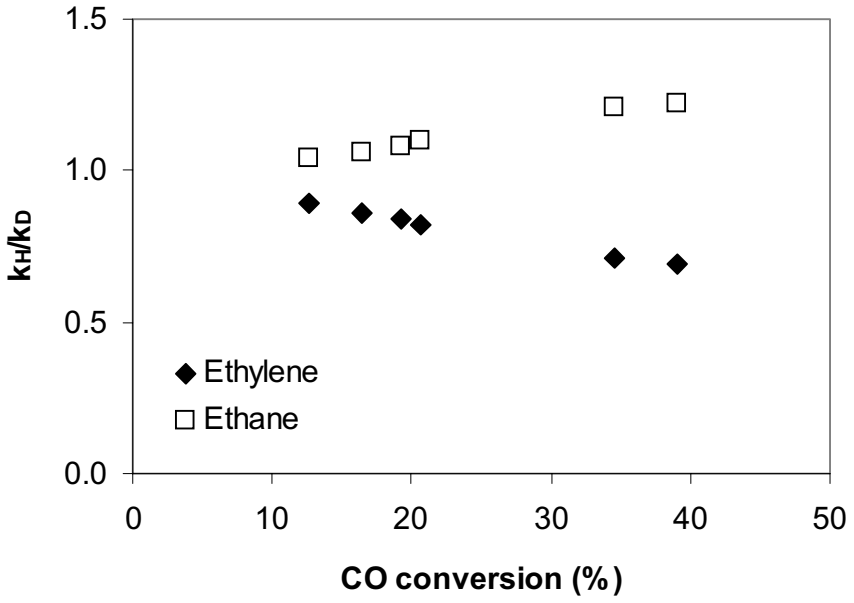

Figure 2.4. Isotope effect for C_2 products versus CO conversion (21.9 wt% Co/SiO_2, 200°C, 20 atm, H_2/CO or D_2/CO = 2.0)

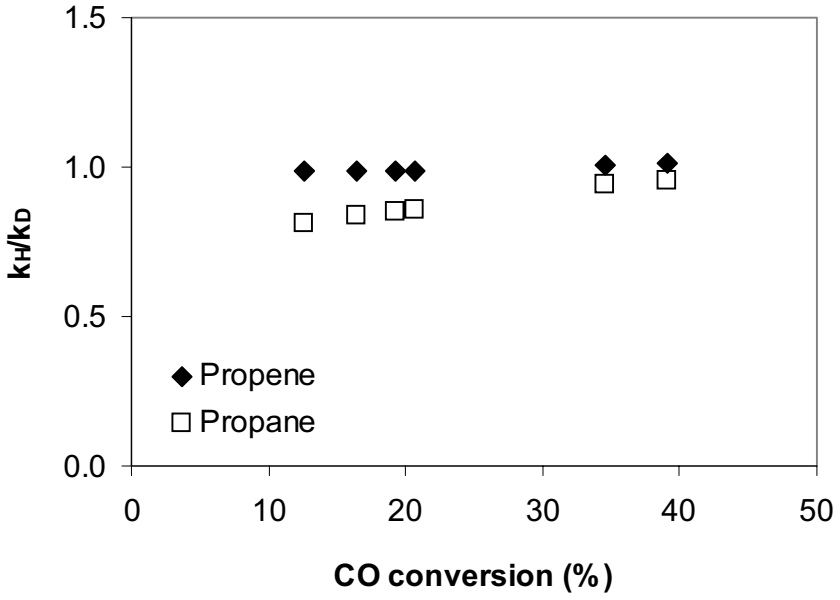

Figure 2.5. Isotope effect for C_3 products versus CO conversion (21.9 wt% Co/SiO_2, 200°C, 20 atm, H_2/CO or D_2/CO = 2.0)

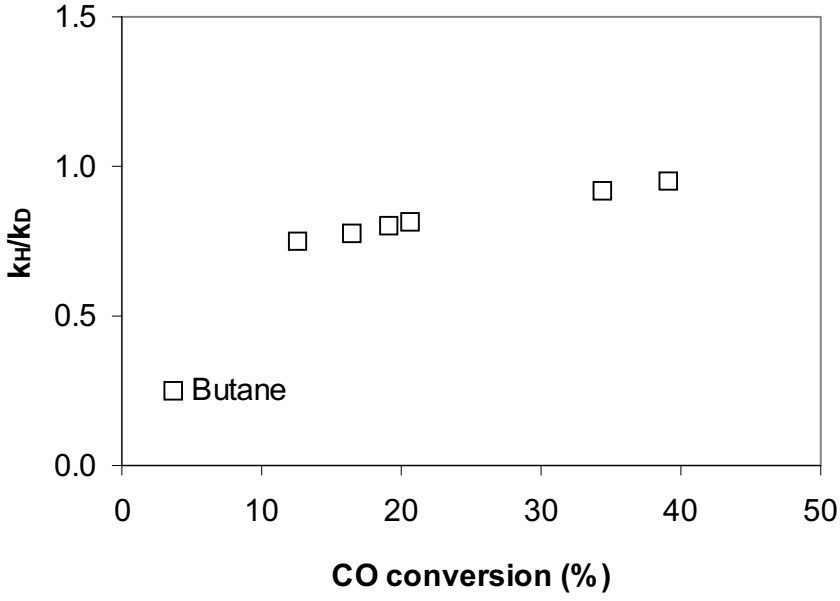

Figure 2.6. Isotope effect for butane versus CO conversion (21.9 wt% Co/SiO_2, 200°C, 20 atm, H_2/CO or D_2/CO = 2.0)

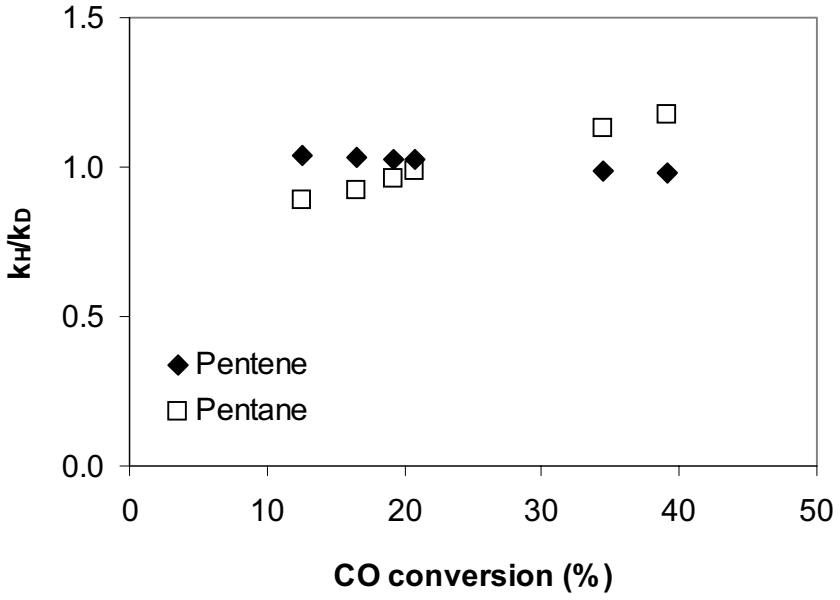

Figure 2.7. Isotope effect for C_5 products versus CO conversion (21.9 wt% Co/SiO_2, 200°C, 20 atm, H_2/CO or D_2/CO = 2.0)

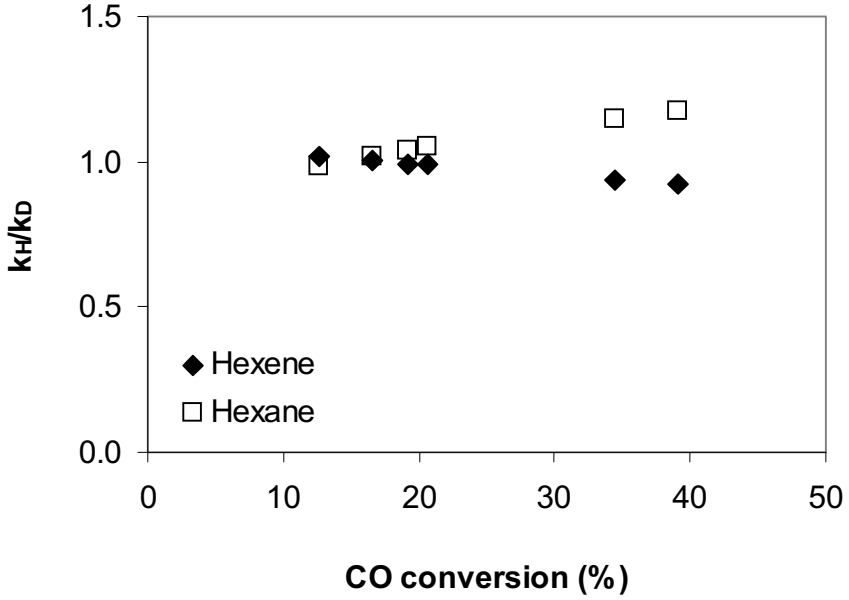

Figure 2.8. Isotope effect for C_6 products versus CO conversion (21.9 wt% Co/SiO_2, 200°C, 20 atm, H_2/CO or D_2/CO = 2.0)

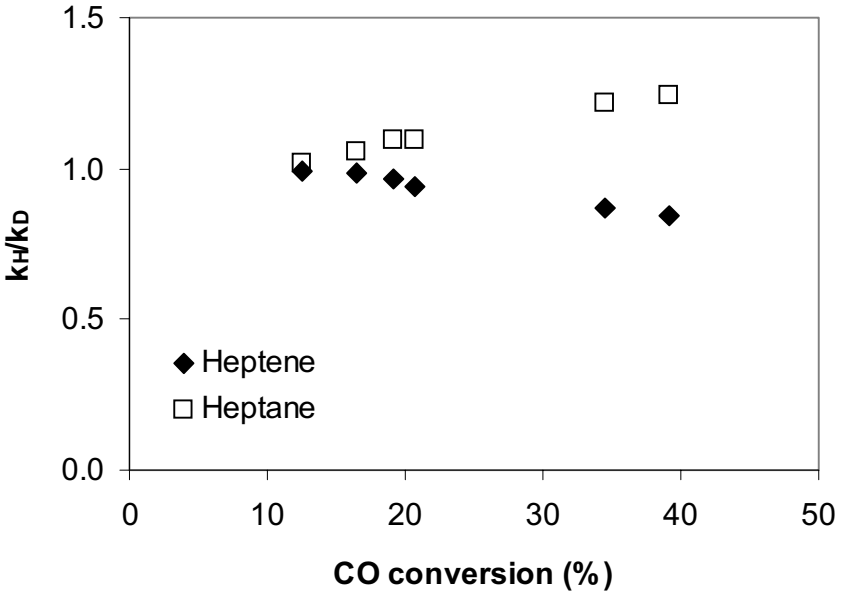

Figure 2.9. Isotope effect for C_7 products versus CO conversion (21.9 wt% Co/SiO_2, 200°C, 20 atm, H_2/CO or D_2/CO = 2.0)

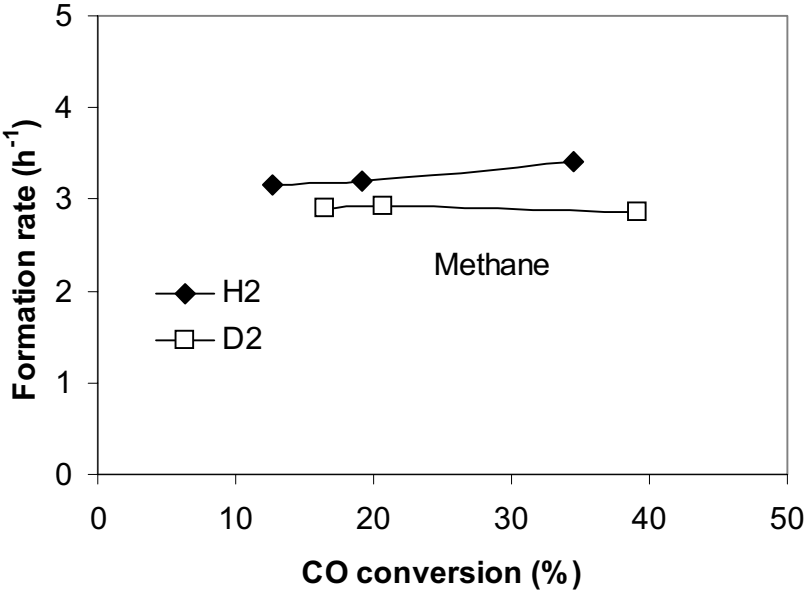

Figure 2.10. Rate of methane formation versus CO conversion (21.9 wt% Co/SiO_2, 200°C, 20 atm, H_2/CO or D_2/CO = 2.0)

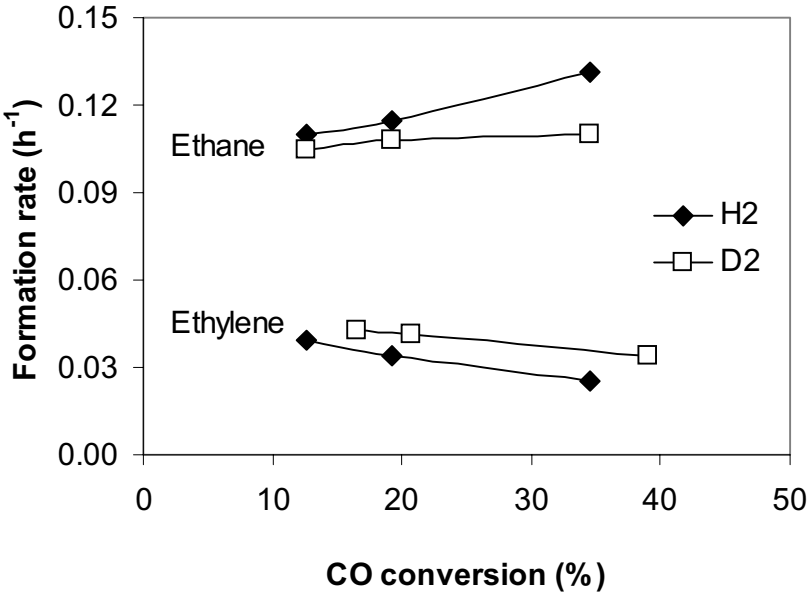

Figure 2.11. Rate of formation of C_2 products versus CO conversion (21.9 wt% Co/SiO_2, 200°C, 20 atm, H_2/CO or D_2/CO = 2.0)

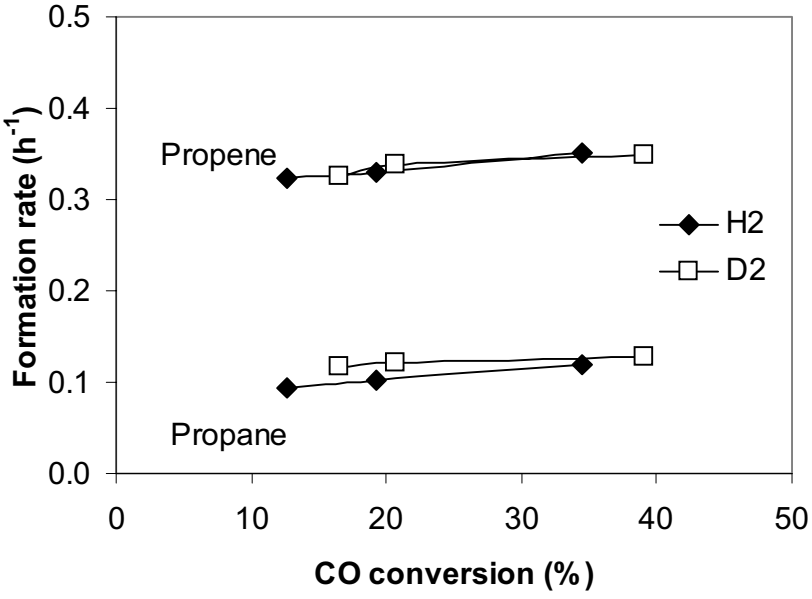

Figure 2.12. Rate of formation of C_3 products versus CO conversion (21.9 wt% Co/SiO_2, 200°C, 20 atm, H_2/CO or D_2/CO = 2.0)

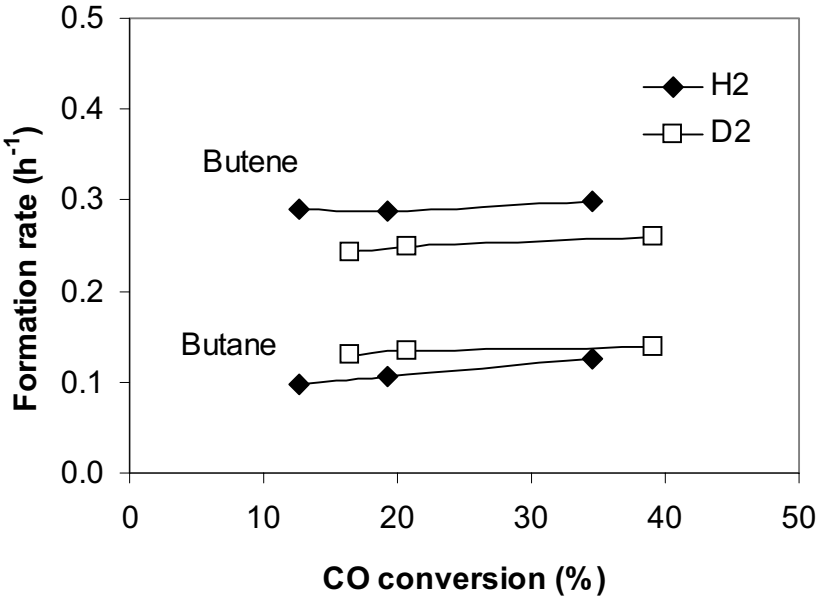

Figure 2.13. Rate of formation of C_4 products versus CO conversion (21.9 wt% Co/SiO_2, 200°C, 20 atm, H_2/CO or D_2/CO = 2.0)

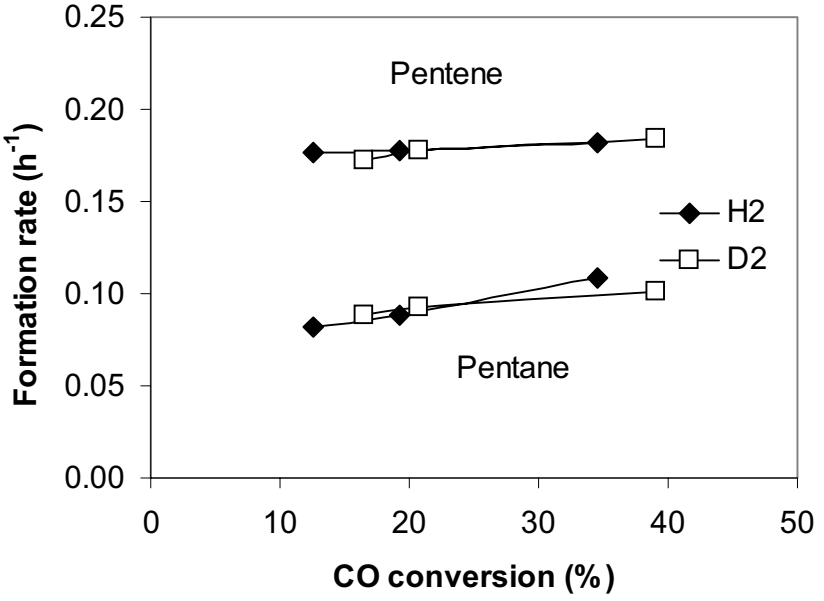

Figure 2.14. Rate of formation of C_5 products versus CO conversion (21.9 wt% Co/SiO_2, 200°C, 20 atm, H_2/CO or D_2/CO = 2.0)

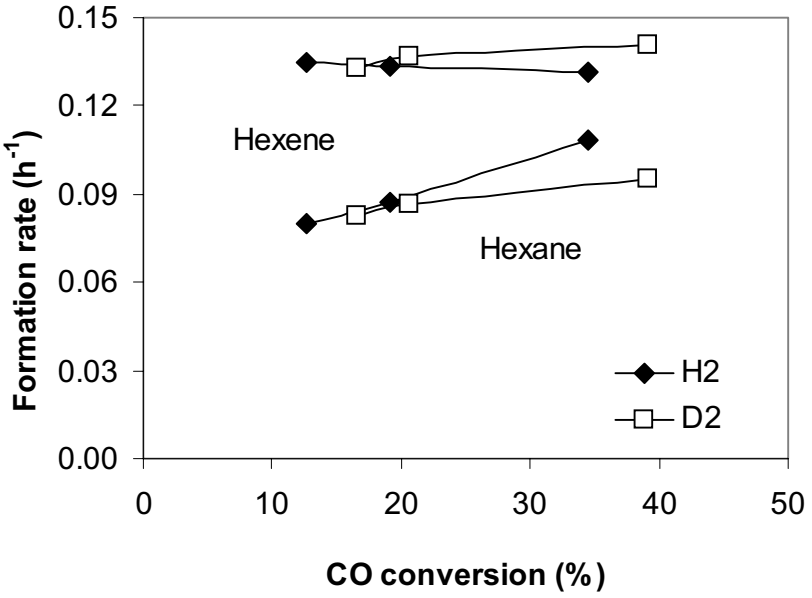

Figure 2.15. Rate of formation of C_6 products versus CO conversion (21.9 wt% Co/SiO_2, 200°C, 20 atm, H_2/CO or D_2/CO = 2.0)

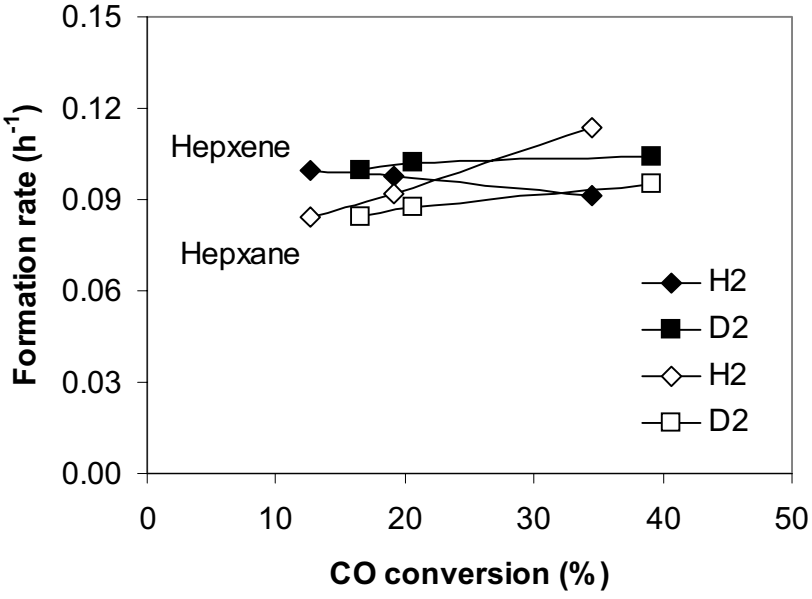

Figure 2.16. Rate of formation of C_7 products versus CO conversion (21.9 wt% Co/SiO_2, 200°C, 20 atm, H_2/CO or D_2/CO = 2.0)

The observed isotope effect for each hydrocarbon may result from a combination of kinetic and equilibrium isotopic effects which arise from individual elementary steps. Thus, the presence or absence of an overall isotope effect cannot be used to identify the rate-determining step [30,31]. But we may explain some of the results qualitatively. As mentioned above, the alkyl groups react to form olefins and paraffins via either hydrogen elimination or addition. The former process favors the reaction of D_2 because formation of a C-D bond is easier. Conversely, the latter process favors the reaction of H_2 because breaking of a C-H bond is easier. Therefore, the observed isotope effects (k_H/k_D) are generally inverse for paraffins whereas normal for olefins when we do not consider the effect of secondary reactions. The isotope effect (k_H/k_D = 0.8) for the overall CO consumption is very close to the effects for paraffins (k_H/k_D = 0.7-0.9, at zero conversion). This is reasonable because the dominant FTS products on Co are paraffins [4].

3.2 Proposed Mechanism

In last quarterly report, we proposed a water-enhanced monomer formation pathway in order to explain the enhancement of the synthesis rate by water observed on cobalt catalysts. In this mechanism, two parallel routes that determine the CO consumption rate were assumed, *i.e.*, adsorbed C* being hydrogenated to form CH* or reacting with adsorbed water to form CHOH* intermediates. A kinetic rate expression was then obtained according to this mechanism.

$$r_{-CO} = aP_{CO}^{1/2}P_{H2}^{1/4}(bP_{H2}^{1/2} + cP_{H2O})^{1/2}/(1 + dP_{H2}^{1/2} + eP_{H2O} + fP_{CO}^{1/2})^2 \qquad (1)$$

During this reporting period, another mechanism was taken into account for the positive water effect. Earlier studies suggest that the surface of Co is covered almost entirely by non-dissociated CO during FTS [26,27]. Hydrogen-assisted CO dissociation has also been considered as a rate-limiting step in FTS [32]. Here, we assumed that both H_2 and H_2O could promote the dissociation of adsorbed CO, which control the CO consumption rate. Then, we have the follow elementary steps.

1. $H_2 + 2* \leftrightarrow 2H*$
2. $CO + * \leftrightarrow CO*$
3. $CO* + H* \rightarrow C* + OH*$
4. $CO* + OH_2* \rightarrow C* + 2OH*$
5. $O* + H* \rightarrow OH* + *$
6. $OH* + H* \rightarrow OH_2* + *$
7. $OH_2* \leftrightarrow H_2O + *$

A rate expression was obtained according to the proposed mechanism,

$$r_{-CO} = (aP_{CO}P_{H2}^{1/2} + bP_{CO}P_{H2O})/(1 + cP_{H2}^{1/2} + dP_{H2O} + eP_{CO})^2, \qquad (2)$$

where,

$a = K_1^{1/2} K_2 k_3$
$b = K_2 k_4 (K_7)^{-1}$
$c = K_1^{1/2}$
$d = (K_7)^{-1}$
$e = K_2$

3.3 FTS Kinetic Study on Co-based Catalysts

Reaction kinetic studies were continued by running FTS with a 21.9 wt% Co/SiO_2 catalyst at 200 ^oC. This time we focused on the effect of water on synthesis rate by adding 0.5-2.0 atm water to the reacting feed (12 atm H_2 and 6 atm CO). CO conversion and selectivities of primary hydrocarbons (up to C_{12}) were measured at steady state. The experimental results are presented in Table 2.1. The overall CO consumption rate data along with those obtained from the previous kinetic run would be fitted to the above two rate expressions with multivariable non-linear regression. We were working on a macro program, which will optimize the regression (using Sigmaplot 5.0) and thus yield the best fit. This may let us distinguish which expression fits our experiment data better.

Table 2.1 Experimental results of FTS kinetic study over a 21.9 wt% Co/SiO_2 catalyst*

No	Partial Pressure (Catalyst Bed, atm)			Syngas Space Velocity	CO Conv	CO Conv Rate	CH_4 Formation Rate
	H_2	CO	H_2O	cc/min	(%)	(h^{-1})	(h^{-1})
1	11.4	5.3	0.6	32.8	20.8	58.3	5.2
2	12.0	5.9	0.2	64.2	5.5	31.2	4.3
3	10.9	2.6	0.3	52.0	19.1	53.6	7.1
4	10.6	2.4	0.4	40.2	28.3	59.0	7.3
5	10.7	1.3	0.2	92.1	22.5	63.1	12.0
6	11.5	8.6	0.3	50.3	6.2	35.2	3.5
7	12.0	5.9	0.2	64.2	5.9	33.5	4.3
8	12.0	5.9	0.8	64.2	9.3	52.8	4.5
9	11.7	5.7	1.3	64.2	11.0	62.5	4.4
10	11.6	5.7	2.4	64.2	12.5	71.0	4.4
11	12.2	5.7	0.2	57.7	6.0	29.8	3.7

* Reaction conditions: 200°C, H_2/CO ratio from 1.3 to 8.5, water partial pressure up to 2 atm, reaction pressure from 13 to 22 atm,

III. REFERENCES

1. M. E. Dry, The Fisher-Tropsch Synthesis, in *Catalysis-Science and Technology*, Vol. 1, p. 160, J. R. Anderson and M. Boudart eds., Springer Verlag, New York, 1981.
2. F. Fischer and H. Tropsch, *Brennstoff-Chem.* **7** (1926) 97.
3. R. B. Anderson, in *Catalysis* Vol. 4, p. 29, P. H. Emmett eds., Van Nostrand-Reinhold, New York, 1956.
4. H. H. Storch, N. Golumbic and R. B. Anderson, *The Fischer-Tropsch and Related Syntheses*, Wiley, New York, 1951; R. B. Anderson, *The Fischer-Tropsch Synthesis*, Wiley, New York, 1984.
5. H. Kolbel and M. Ralek, *Catal. Rev.-Sci. Eng.* **21** (1980) 225.
6. J. W. Niemantsverdriet and A. M. van der Kraan, *J. Catal.* **72** (1981) 385.
7. J. A. Amelse, J. B. Butt and L. J. Schwartz, *J. Phys. Chem.* **82** (1978) 558.
8. G. B. Raupp and W. N. Delgass, *J. Catal.* **58** (1979) 348.
9. R. Dictor and A. T. Bell, *J. Catal.* **97** (1986) 121.
10. J. P. Reymond, P. Meriaudeau and S. J. Teichner, *J. Catal.* **75** (1982) 39.
11. C. S. Kuivila, P. C. Stair and J. B. Butt, *J. Catal.* **118** (1989) 299.
12. C. S. Huang, L. Xu and B. H. Davis, *Fuel Sci. Tech. Int.* **11** (1993) 639.
13. E. Iglesia, and S. C. Reyes, R. J. Madon and S. L. Soled, *Advances in Catalysis*, Vol. 39, p. 221, Academic Press, 1993.
14. E. Iglesia, *Appl. Catal. A: General* **161** (1997) 59.
15. S. Soled, E. Iglesia and R. A. Fiato, *Catal. Lett.* **7** (1990) 271.
16. S. Soled, E. Iglesia, S. Miseo, B. A. DeRites and R. A. Fiato, *Topics in Catal.* **2** (1995) 193.
17. E. Iglesia, A research proposal submitted to the Division of Fossil Energy.
18. M. T. Xu, E. Iglesia, *J. Phys. Chem. B* **102(6)**, 961-966, 1998.
19. A. P. Raje, R. J. O'Brien and B. H. Davis, *J. Catal.* **180** (1998) 36.
20. A. F. Wells, *Structural Inorganic Chemistry*, Oxford, 1945.
21. T. P. Wilson, *J. Catal.* **60**, 167 (1979).
22. T. Soller, S. Goldwasser and R.A. Beebe, *J. Am. Chem. Soc.,* **58**, 1703 (1936).
23. F. de Pauw, J. C. Jungers, *Bull. Soc. Chim. Belg*., **57**, 618 (1948).
24. J. Nicolai, M. Hont and J.C. Jungers, *Bull. Soc. Chim. Belg*., **55**, 160 (1946).
25. G. A Huff, and C. N. Satterfild, *Ind. Eng. Chem. Res.* **23**, 696 (1984).
26. H. H. Storch, N. Golumbic and R. B. Anderson, *The Fischer-Tropsch and Related Syntheses*, Wiley, New York, 1951; R. B. Anderson, *The Fischer-Tropsch Synthesis*, Wiley, New York, 1984.
27. A. T. Bell, *Catal. Rev. Sci. Eng*. **23 (1&2)** (1981) 203.
28. M. M., Sakharov and E. S., Dokukina, *Kinet. Katal*. **2** (1961) 710.
29. D. W., Mckee, *J. Catal.* **8** (1967) 240.
30. T. P., Wilson, *J. Catal.* **60** (1979) 167.
31. C. S., Kellner and A. T. Bell, *J. Catal.* **67** (1981) 175.
32. H. H. Nijs, and P. A. Jacobs, *J. Catal.* **66** (1980) 401.

Task 12. Reporting/Project Management

One quarterly and three monthly reports have been completed.